



HAL
open science

Revisiting the Luminescence Properties of Er^{3+} , Tm^{3+} and Ho^{3+} Doped $\text{Bi}_4\text{Ge}_3\text{O}_{12}$ Rod-Type Crystal Fibers for the Laser Application

Jie Xu, Yannick Guyot, Abdeldjelil Nehari, Kheirreddine Lebbou, Xiaodong Xu, Jian Liu, Jun Xu, Richard Moncorgé

► To cite this version:

Jie Xu, Yannick Guyot, Abdeldjelil Nehari, Kheirreddine Lebbou, Xiaodong Xu, et al.. Revisiting the Luminescence Properties of Er^{3+} , Tm^{3+} and Ho^{3+} Doped $\text{Bi}_4\text{Ge}_3\text{O}_{12}$ Rod-Type Crystal Fibers for the Laser Application. *Journal of Luminescence*, 2023, 226, pp.120238. 10.1016/j.jlumin.2023.120238 . hal-04298112

HAL Id: hal-04298112

<https://hal.science/hal-04298112>

Submitted on 12 Jan 2024

HAL is a multi-disciplinary open access archive for the deposit and dissemination of scientific research documents, whether they are published or not. The documents may come from teaching and research institutions in France or abroad, or from public or private research centers.

L'archive ouverte pluridisciplinaire **HAL**, est destinée au dépôt et à la diffusion de documents scientifiques de niveau recherche, publiés ou non, émanant des établissements d'enseignement et de recherche français ou étrangers, des laboratoires publics ou privés.

Revisiting the luminescence properties of Er³⁺, Tm³⁺ and Ho³⁺ doped Bi₄Ge₃O₁₂ rod-type crystal fibers for the laser application

Jie Xu¹, Y. Guyot¹, A. Nehari¹, K. Lebbou¹, Xiaodong Xu², Jian Liu³, Jun Xu³,
R. Moncorgé⁴

¹*Institut Lumière Matière (ILM), UMR 5306 Université Lyon1-CNRS, Université de Lyon, Lyon 69622, Villeurbanne Cedex, France*

²*Jiangsu Key Laboratory of Advanced Laser Materials and Devices, School of Physics and Electronic Engineering, Jiangsu Normal University, Xuzhou 221116, China*

³*School of Physics Science and Engineering, Institute for Advanced Study, Tongji University, Shanghai 200092, China*

⁴*Centre Interdisciplinaire de recherche sur les Matériaux et la Photonique (CIMAP), UMR 6252 CEA-CNRS-ENSICAEN, Université de Caen Normandie, 14050 Caen, France*

Corresponding authors: yannick.guyot@univ-lyon1.fr, richard.moncorge@ensicaen.fr

Abstract:

BGO single crystals doped with Er³⁺, Tm³⁺ and Ho³⁺ rare-earth ions were prepared in the form of rod-type crystal fibers via the micro-pulling down technique to perform an extensive investigation of their visible, near- and mid-infrared luminescence properties and to really decide on their interest as solid-state laser media in the various spectral domains. Revisiting and completing the absorption spectra already available in the literature led to the derivation of more reliable “effective” radiative lifetimes and branching ratios. Registration of the fluorescence decays of the most important emitting levels versus dopant concentrations led for the first time to an unambiguous determination of “intrinsic” emission lifetimes – corresponding to negligible contributions from inter-ionic energy-transfers - and non-radiative multiphonon relaxation rates. Such data also allowed for the determination of the dominant phonon energy which comes into play in the electron-phonon coupling responsible for these multiphonon relaxation processes and for its lattice vibration origin, i.e. a high phonon energy of the order of 820 cm⁻¹ corresponding to the coupling between bending vibrations of (GeO₄)⁴⁻ tetrahedra and vibrations corresponding to motions of these (GeO₄)⁴⁻ tetrahedra against the Bi³⁺ ions for which the rare-earth dopant ions substitute. Using the above data and different methods for the calibration of the registered emission spectra in cross section unit and for the derivation of gain cross section curves finally show that mid-infrared emissions of Er:BGO, Tm:BGO and Ho:BGO around 1.55 μm, 1.9 μm and 2 μm, respectively, occur with comparable gain cross sections as in the most important reference mid-infrared laser materials, although over slightly shifted thus complementary spectral domains. It is shown that potentialities also exist with Tm:BGO in the blue, deep-red and near-infrared spectral domains around 470 nm, 800 nm and 1.45 μm, by pumping the crystals with conventional pump sources and using some suitable co-dopants to avoid detrimental self-terminating processes.

Keywords: Bi₄Ge₃O₁₂, Erbium, Thulium, Holmium, Micro-pulling-down, Spectroscopy

1. Introduction

Thanks to a low melting temperature of about 1045°C and a well-mastered crystal growth [1] plus a number of favourable physical and spectral properties [2-4] such as a high-density (7 g/cm³), broad absorption and emission bands in the near-UV and visible spectral regions together with a short emission lifetime (around 300 ns at room temperature), undoped Bismuth Germanate Bi₄Ge₃O₁₂ (BGO) is a well-known scintillation material which is widely and successfully used in a large number of applications in the fields of high energy physics, nuclear medicine and detection science and technology [5-10]. Undoped BGO was also recently found as a promising high-capacity lithium-ion battery anode for energy storage applications [11].

BGO crystals doped with transition metals of the iron group such as Cr, Mn, Fe and Co were studied for their photochromic and photorefractive behavior and their potential use in the production of optically induced holographic gratings [12-15].

BGO can also be doped rather easily with trivalent rare-earth ions and some of these rare-earth doped materials were investigated for lighting [16-18], temperature sensing [19] scintillating [20-22] and laser applications [23-31], the latter more specifically not only because of favorable emission properties but also because of several excellent optical, electro-optic and thermo-mechanical properties [23, 32-34] and because very stable, non-hygroscopic and high optical quality single crystals can be obtained in the form of large-size bulk materials as well as sub-millimeter rod-type crystal fibers by using well-mastered and low-temperature crystal growth techniques [1, 35-37]. This is not the case of many well-known reference laser materials for high power laser applications such as YLF (LiYF₄), YAG (Y₃Al₅O₁₂), YAP (YAlO₃) and (Y,Lu)₂O₃.

Despite of that, to the best of our knowledge, only the spectroscopic properties of Nd³⁺ were thoroughly enough investigated and Nd³⁺-doped BGO crystals (in the form of crystal fibers) could be lased efficiently, moreover in continuous mode [26]. Concerning the spectroscopic properties of Er³⁺, Tm³⁺ and Ho³⁺ ions in BGO, which is the subject of the present investigation, there is no such detailed and systematic experimental and theoretical study, and/or there are still some missing data and unanswered questions to be clarified, especially that concerning the electron-phonon coupling and the non-radiative multi-phonon relaxation mechanisms affecting the emission lifetimes and quantum yields of the excited emitting levels. For instance, there is still some ambiguity as to the vibrational origin and the effective phonon energy [23, 27, 37, 39] which have to be invoked in these mechanisms.

Therefore, in the present work, we addressed the above issues (i) by revisiting and completing the absorption spectra already available in the literature, to offer the reader more usable data, and by analyzing these spectra more carefully within the framework of the Judd-Ofelt- formalism, in order to derive the most reliable radiative lifetimes and branching ratios of the most important emitting levels and associated emission transitions, (ii) by recording the corresponding emission spectra and fluorescence lifetimes, in order to re-examine the non-radiative multi-phonon relaxation parameters which were proposed in the past, and to finally show the interest of Er³⁺, Tm³⁺ and Ho³⁺-doped BGO crystals as solid-state laser materials in the mid-infrared but also in the visible and near-infrared spectral domains.

The paper is organized as follows. Crystal growth and experimental techniques are described in Section 2. Absorption data are presented and analyzed in Section 3. Emission spectra are presented exploited in Section 4. Fluorescence decay measurements and non-radiative multiphonon relaxation considerations are gathered in Section 5. Analysis and

discussion of the results are presented in Section 6, and conclusions are presented in Section 7.

2. Crystal growth and experimental techniques

2.1. Growth and structural characteristics of rare-earth doped $\text{Bi}_4\text{Ge}_3\text{O}_{12}$ crystal fibers

$\text{RE}_{4x}\text{Bi}_{4(1-x)}\text{Ge}_3\text{O}_{12}$ crystalline fibers with $x = 0.5\text{at.}\%$ for Er:BGO and Ho:BGO, and $x = 0.5, 0.75, 1, 1.5$ and $2\text{at}\%$ for Tm:BGO, were prepared by using the μ -PD method [16-18, 26, 27, 35-37]. 99.999% purity Bi_2O_3 , GeO_2 , Er_2O_3 , Tm_2O_3 , and Ho_2O_3 powders were used as starting materials. The crystals were grown by melting the powders at about 1045°C in a Pt crucible and by pulling the fibers through a capillary channel using a pulling rate of $0.3\text{mm}/\text{min}$ in air atmosphere; their diameter was maintained constant by controlling the power and the pulling rate [31]. In this way, high optical quality 2 mm diameter and 50 mm long rod-type crystal fibers could be grown rather easily. Spectroscopic measurements were performed by using 2 mm long samples with polished end-faces.

BGO is a cubic system (space group $T_d^6 = I43d$) [23, 40, 41] which remains so when it is doped with small amounts of trivalent rare-earth ions. Whatever their ionic radius (1.00 \AA for Nd^{3+} , 0.88 \AA for Er^{3+} , 0.87 \AA for Tm^{3+} and 0.89 \AA for Ho^{3+}) they easily substitute for Bi^{3+} ions (0.96 \AA) the ones occupy non-equivalent but very similar quasi-trigonal (distorted octahedra) C_3 symmetry sites [20, 23, 25, 42]. Thanks to that and to the particular growth process Er^{3+} , Tm^{3+} and Ho^{3+} dopants could be incorporated inside the crystals with a segregation coefficient nearly equal to 1.

2.2. Spectroscopic measurements

Absorption spectra were registered between 300 nm and 2400 nm by using a standard Perkin-Elmer (PE) double-beam Lambda 900 UV/VIS/NIR spectrophotometer. Emission spectra were registered by exciting the crystals with an EKSPLA NT342B tunable OPO (Optical Parametric Oscillator) pumped by a pulsed and frequency-tripled Nd:YAG laser delivering 7 ns laser pulses of a few mJ at a 10Hz repetition rate or by exciting them with CW (continuous wave) LEDs from THORLABS. Time-resolved and continuous emission signals were dispersed and detected in the visible range with the aid of a SHAMEROCK 350 monochromator and an ANDOR ICCD gated detector. In the NIR (near-infrared) range, emission spectra were recorded using an ANDOR InGaAs iDus CCD camera (for $\lambda < 1700$ nm) or a JUDSON InGaAs nitrogen cooled G7754-03 detector, following a SHAMEROCK 500i monochromator equipped with $1 \mu\text{m}$ and $1.9 \mu\text{m}$ blazed gratings, respectively. Most of the spectra were corrected for the spectral response of the equipment using a calibrated ORIEL halogen lamp. Fluorescence decay measurements were performed by using the same laser excitation sources and monochromators as above and by analyzing the signals with the help of R928 AsGa (RESEARCH Inc.) and NIR H10330B-75 InP/InGaAs (HAMAMATSU) photomultiplier tubes coupled with a Wave Runner 64Xi LECROY digital scope, for the visible and NIR spectral ranges, respectively.

3. Absorption spectra and Judd-Ofelt analysis

The absorption spectra of the 0.5%Er:BGO, 2%Tm:BGO and 0.5%Ho:BGO crystals are reported in the figures 1 to 3, knowing that a dopant concentration of 1 at.% corresponds to an ion density of about 1.368×10^{20} ions/cm³⁺.

The energy level schemes and the most important emission transitions observed with each rare-earth ion in BGO are displayed in Fig. 4.

Case of Er:BGO

The absorption spectrum of Er³⁺:BGO has been registered between 320 and 1700 nm. As shown in Fig. 1, most of the absorption structures can be assigned to absorption transitions from the ⁴I_{15/2} ground level to well-defined excited multiplets. Some of them, however, more particularly in the short wavelength domain, correspond to several overlapping transitions.

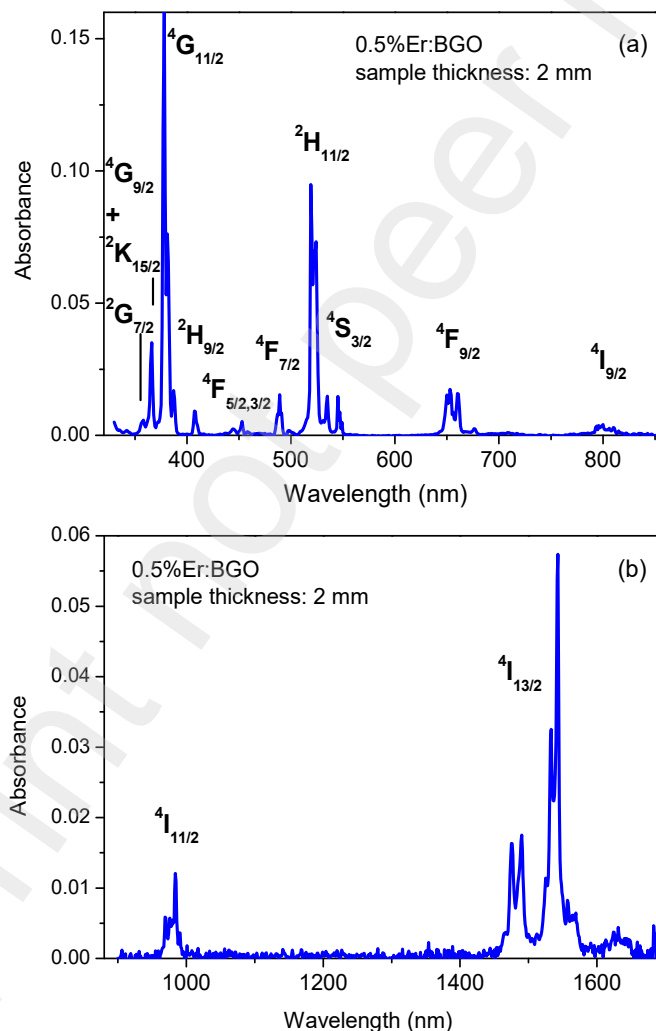


Fig. 1. Room temperature absorbance (optical density) of a 2.0 mm thick 0.5%Er³⁺ doped BGO sample (a) in the visible and (b) in the infrared spectral domains

A similar spectrum was already reported in the past [30] but without providing any absorption scale. However, most of the important transitions (up the ⁴I_{15/2}→⁴S_{3/2} transition around 540

nm) were studied at liquid-nitrogen temperature (LNT), allowing for the determination of the Stark levels energies and the partition functions of all the corresponding multiplets, what will be used in the following (see in Section 6) to derive stimulated emission cross section spectra starting from absorption data by using the so-called “Reciprocity” or McCumber method..

The above absorption spectrum was then analyzed within the framework of the Judd-Ofelt (J.O.) formalism, as in [30], but including in our analysis all the absorption transitions up to the $^4I_{15/2} \rightarrow ^2H_{9/2}$ transition around 408 nm and by using the electric-dipole (ED) and magnetic-dipole (MD) transition matrix elements reported in [43]. The refractive index variation (dispersion relation) used in the calculations was that presented in [33].

Table 1. Electric-dipole (ED) and Magnetic-dipole (MD) emission rates along with radiative emission lifetimes τ_R and branching ratios β_R for Er^{3+} doped BGO; Also put in parentheses the “effective” radiative emission lifetime (see in the text) of the thermalized emitting levels $^4S_{3/2}(^2H_{11/2})$

Emission transition	Average emission wavelength (nm)	ED emission transition rate (s ⁻¹)	MD emission transition rate (s ⁻¹)	Branching ratio β_R (%)	Radiative lifetime τ_R (ms)
$^4I_{13/2} \rightarrow ^4I_{15/2}$	1553	57.33	82.92	100	7.13
$^4I_{11/2} \rightarrow ^4I_{15/2}$	990	85.58	0	74.3	8.68
$\rightarrow ^4I_{13/2}$	2770	10.75	18.81	25.7	
$^4F_{9/2} \rightarrow ^4I_{15/2}$	660	995.07	0	90.0	0.90
$\rightarrow ^4I_{13/2}$	1160	50.92	0	4.6	
$\rightarrow ^4I_{11/2}$	1990	36.86	13.29	4.4	
$\rightarrow ^4I_{9/2}$	3580	3.30	5.53	0.8	
$^4S_{3/2} \rightarrow ^4I_{15/2}$	552	646.86	0	68.8	1.06 (0.75)
$\rightarrow ^4I_{13/2}$	856	240.82	0	25.6	
$\rightarrow ^4I_{11/2}$	1240	19.21	0	2.0	
$\rightarrow ^4I_{9/2}$	1710	33.32	0	3.5	
$\rightarrow ^4F_{9/2}$	3276	0.26	0	0.3	
$^2H_{11/2} \rightarrow ^4I_{15/2}$	521	6920	0	94.3	0.136
$\rightarrow ^4I_{13/2}$	792	100.79	143.12	3.3	
$\rightarrow ^4I_{11/2}$	1124	54.93	17.48	0.9	
$\rightarrow ^4I_{9/2}$	1488	75.15	1.43	1.0	
$\rightarrow ^4F_{9/2}$	2532	23.68	0.30	0.3	
$\rightarrow ^4S_{3/2}$	1198	0.03	0	0.04	

The best fit to the data was obtained, by gathering the strongly overlapping $^4I_{15/2} \rightarrow ^4F_{5/2,3/2}$, $^4I_{15/2} \rightarrow ^2H_{11/2} + ^4S_{3/2}$ transitions around 450 nm and 530 nm (see in Fig. 1), respectively, for the J.O. parameters:

$$\Omega_2 = 1.916 \times 10^{-20} \text{ cm}^2, \Omega_4 = 0.531 \times 10^{-20} \text{ cm}^2, \Omega_6 = 0.266 \times 10^{-20} \text{ cm}^2$$

with the root-mean-square (rms) deviation $\delta = 0.044 \times 10^{-20} \text{ cm}^2$. The calculated ED and MD transition rates (spontaneous emission probabilities) and the resulting radiative emission lifetimes and branching ratios are reported in Table 1. Of particular interest in the following sections is the ${}^4I_{13/2}$ radiative emission lifetime of 7.13 ms (7.8 ms according to [30]).

Case of Tm:BGO

The room temperature absorption spectrum of $\text{Tm}^{3+}:\text{BGO}$ has been registered between 320 and 2100 nm. As previously, most of the absorption structures could be assigned to absorption transitions between the ${}^3\text{H}_6$ ground level and well-defined excited multiplets (see in Fig. 2), the most important ones for the mid-infrared laser application peaking around 791 nm (${}^3\text{H}_6 \rightarrow {}^3\text{H}_4$ transition) and 1738 nm (${}^3\text{H}_6 \rightarrow {}^3\text{F}_4$ transition). A similar spectrum was also reported in the past [30, 31] but with much less clear absorption profiles and without reporting the Stark level structure of any multiplet.

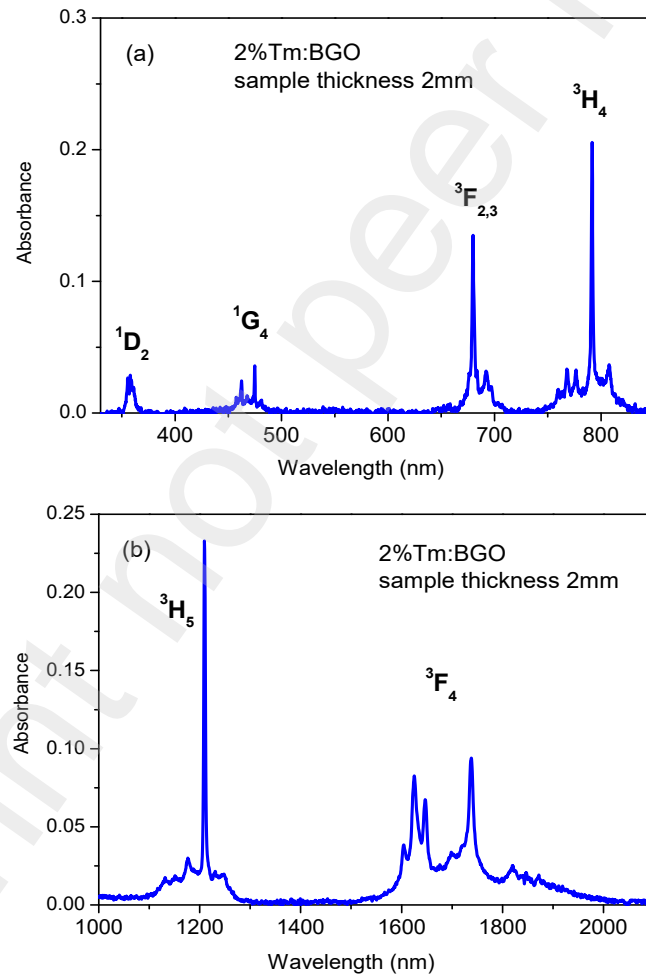


Fig. 2. Room temperature absorbance (optical density) of a 2.0 mm thick 2%Tm³⁺ doped BGO sample (a) in the visible and (b) in the infrared spectral domains

This absorption spectrum was also analyzed within the framework of the Judd-Ofelt formalism without using the absorption data for the ${}^3\text{H}_6 \rightarrow {}^3\text{H}_5$ transition around 1200 nm, by gathering the data for the ${}^3\text{H}_6 \rightarrow {}^3\text{F}_2$ and ${}^3\text{F}_3$ transitions around 680 nm, and by using the revisited transition matrix elements and the procedure described in [44]. The refractive index variation (dispersion relation) used in the calculations was again that reported in [33]. The best fit to the data was obtained for the Judd-Ofelt parameters:

$$\Omega_2 = 2.125 \times 10^{-20} \text{ cm}^2, \Omega_4 = 0.639 \times 10^{-20} \text{ cm}^2 \text{ and } \Omega_6 = 0.150 \times 10^{-20} \text{ cm}^2$$

with $\delta = 0.070 \times 10^{-20} \text{ cm}^2$

The transition rates and the resulting radiative emission lifetimes and branching ratios for the various emission transitions are reported in Table 2. Of particular interest in the following sections are the ${}^3\text{F}_4$ and ${}^3\text{H}_4$ radiative emission lifetimes of 5.63 ms (6.6 ms according to [30]) and 1.00 ms, respectively, and a branching ratio for the ${}^3\text{H}_4 \rightarrow {}^3\text{F}_4$ emission transition around 1460 nm of about 11.5%.

Table 2. Electric-dipole (ED) and Magnetic-dipole (MD) emission rates along with radiative emission lifetimes τ_R and branching ratios β_R for Tm^{3+} doped BGO.

Emission transition	Emission wavelength (nm)	ED emission transition rate (s^{-1})	MD emission transition rate (s^{-1})	Branching ratio β_R (%)	Radiative lifetime τ_R (ms)
${}^3\text{F}_4 \rightarrow {}^3\text{H}_6$	1850	177.5	0	100	5.63
${}^3\text{H}_5 \rightarrow {}^3\text{H}_6$	1235	139.3	116.9	98.6	3.85
$\rightarrow {}^3\text{F}_4$	4080	3.4	0.26	1.4	
${}^3\text{H}_4 \rightarrow {}^3\text{H}_6$	805	856.63	0	85.6	1.00
$\rightarrow {}^3\text{F}_4$	1460	84.2	30.8	11.5	
$\rightarrow {}^3\text{H}_5$	2350	17.5	12.3	2.9	
${}^1\text{G}_4 \rightarrow {}^3\text{H}_6$	482	899.1	0	52.6	0.585
$\rightarrow {}^3\text{F}_4$	665	70.9	13.6	4.9	
$\rightarrow {}^3\text{H}_5$	795	317.8	179.7	29.1	
$\rightarrow {}^3\text{H}_4$	1205	149.7	43.0	11.3	
$\rightarrow {}^3\text{F}_{2,3}$	1600	20.6	4.4	1.5	
${}^1\text{D}_2 \rightarrow {}^3\text{H}_6$	370	5201.6	0	19.9	0.038
$\rightarrow {}^3\text{F}_4$	457	1694.8	0	65.0	
$\rightarrow {}^3\text{H}_5$	520	30.9	0	0.1	
$\rightarrow {}^3\text{H}_4$	672	1627.7	0	6.2	
$\rightarrow {}^3\text{F}_{2,3}$	780	1876.0	205.6	7.9	
$\rightarrow {}^1\text{G}_4$	1520	173.5	0	0.7	

Case of Ho:BGO

The room-temperature absorption spectrum of Ho:BGO has been registered between 320 and 2200 nm. A similar spectrum was also reported in the past [30] but with much less clear absorption profiles, without providing any absorption scale and without reporting the Stark level structure of any multiplet. The spectrum consists of 10 groups of lines assigned according to the sequence of energy levels and absorption transitions given in [45], i.e. $^5I_8 \rightarrow ^3H_5 + ^3H_6$ around 361 nm, $^5I_8 \rightarrow ^5G_4 + ^3K_7$ around 386 nm, $^5I_8 \rightarrow ^5G_5 + ^3G_5$ around 415 nm, $^5I_8 \rightarrow ^5G_6 + ^5F_1$ around 455 nm, $^5I_8 \rightarrow ^5F_{3,2} + ^3K_8$ around 488 nm, $^5I_8 \rightarrow ^5F_4 + ^5S_2$ around 540 nm, $^5I_8 \rightarrow ^5F_5$ around 650 nm, $^5I_8 \rightarrow ^5I_5$ around 915 nm, $^5I_8 \rightarrow ^5I_6$ around 1175 nm and $^5I_8 \rightarrow ^5I_7$ around 1945 nm. No trace of $^5I_8 \rightarrow ^5I_4$ absorption line could be found around the expected wavelength of 750 nm.

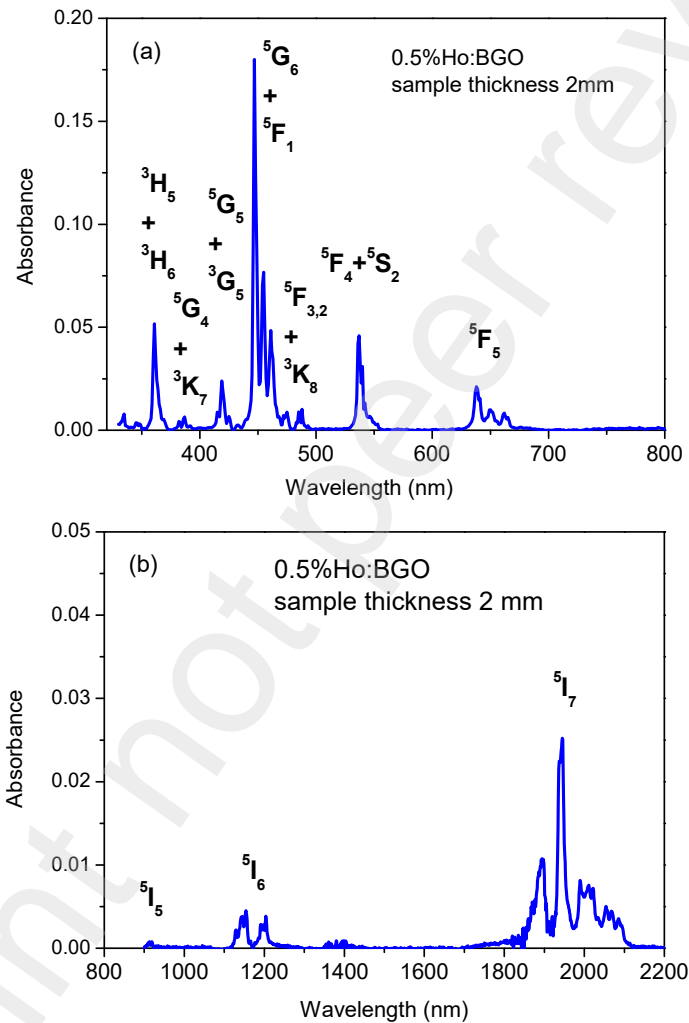


Fig. 3. Room temperature absorbance (optical density) of a 2.0 mm thick 0.5%Ho³⁺ doped BGO sample (a) in the visible and (b) in the infrared spectral domains

The absorption spectrum was then analyzed within the framework of the Judd-Ofelt formalism by using the ED transition matrix elements given in [45, 46] and the MD transition matrix elements derived from the MD transition rates reported in [47]. The refractive index variation (dispersion relation) used in the calculations was again that reported in [33]. By discarding the $^5I_8 \rightarrow ^3H_5 + ^3H_6$ around 361 nm and gathering the strongly overlapping

${}^5I_8 \rightarrow {}^5G_4 + {}^3K_7$, ${}^5I_8 \rightarrow {}^5G_5 + {}^3G_5$, ${}^5I_8 \rightarrow {}^5G_6 + {}^5F_1$, ${}^5I_8 \rightarrow {}^5F_{3,2} + {}^3K_8$ and ${}^5I_8 \rightarrow {}^5F_4 + {}^5S_2$ transitions, respectively, the best fit to the data was obtained for the J.O. parameters:

$$\Omega_2 = 1.61 \times 10^{-20} \text{ cm}^2, \Omega_4 = 1.053 \times 10^{-20} \text{ cm}^2 \text{ and } \Omega_6 = 0.245 \times 10^{-20} \text{ cm}^2$$

with $\delta = 0.168 \times 10^{-20} \text{ cm}^2$. The derived ED and MD emission transition rates and the resulting radiative emission lifetimes and branching ratios are reported in Table 3.

Table 3. Electric-dipole (ED) and Magnetic-dipole (MD) emission rates along with radiative emission lifetimes τ_R and branching ratios β_R for Ho^{3+} doped BGO; Also put in parentheses the “effective” radiative emission lifetime (see in the text) of the thermalized emitting levels ${}^5S_2({}^5F_4)$.

Emission transition	Emission wavelength (nm)	ED emission transition rate (s^{-1})	MD emission transition rate (s^{-1})	Branching ratio β_R (%)	Radiative lifetime τ_R (ms)
${}^5I_7 \rightarrow {}^5I_8$	1980	29.54	42.98	100	13.78
${}^5I_6 \rightarrow {}^5I_8$	1190	64.52	0	67.8	10.56
$\rightarrow {}^5I_7$	2941	7.84	22.83	32.2	
${}^5F_5 \rightarrow {}^5I_8$	664	1249	0	77.3	0.62
$\rightarrow {}^5I_7$	966	313.26	0	19.4	
$\rightarrow {}^5I_6$	1460	48.79	0	3.0	
$\rightarrow {}^5I_5$	2325	3.57	0	0.2	
$\rightarrow {}^5I_4$	4444	0.04	0	0.002	
${}^5S_2 \rightarrow {}^5I_8$	550	480.3	0	52.9	
$\rightarrow {}^5I_7$	755	310.2	0	34.1	
$\rightarrow {}^5I_6$	1015	72.8	0	8.0	
$\rightarrow {}^5I_5$	1369	14.9	0	1.6	
$\rightarrow {}^5I_4$	1950	16.4	0	1.8	
$\rightarrow {}^5F_5$	3340	13.6	0	1.5	
${}^5F_4 \rightarrow {}^5I_8$	540	2176	0	75.2	0.34
$\rightarrow {}^5I_7$	740	397.8	0	13.7	
$\rightarrow {}^5I_6$	995	228.4	0	7.9	
$\rightarrow {}^5I_5$	1340	74.2	0	2.5	
$\rightarrow {}^5I_4$	1904	8.8	0	0.3	
$\rightarrow {}^5F_5$	3190	8.7	8	0.6	

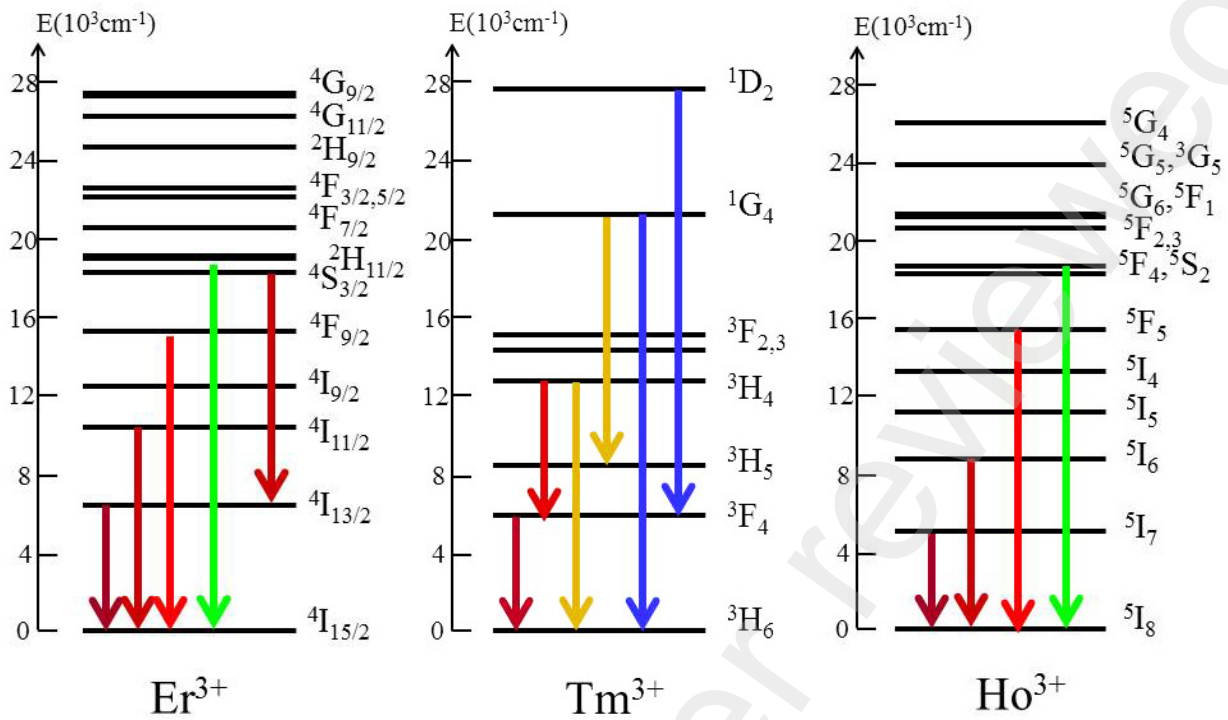


Fig. 4. Energy level schemes and most intense emission transitions observed in Er:BGO, Tm:BGO and Ho:BGO

4. Spectral characteristics of the main emission transitions

In the case of **Er:BGO**, as in most of the Er^{3+} doped oxides, and according to the branching ratios reported in Table 1, the most important emission transitions (see in Fig. 4) should originate from the $^4\text{S}_{3/2}$ and $^4\text{F}_{9/2}$ emitting levels with emissions in the green ($\lambda \approx 552$ nm, $\beta \approx 68.8\%$), in the red ($\lambda \approx 660$ nm, $\beta \approx 90\%$) and in the near-infrared ($\lambda \approx 856$ nm, $\beta \approx 25.6\%$), and from the $^4\text{I}_{13/2}$ metastable level with a mid-infrared emission around 1553 nm. The emissions coming from the $^4\text{I}_{11/2}$ level should only appear if the electron-phonon coupling is relatively weak and the phonons involved in the multiphonon relaxation process are sufficiently low, a question which will be more particularly addressed in Section 5.

Consequently, emission spectra were registered first by exciting the sample at about 519 nm, i.e. in the $^2\text{H}_{11/2}$ energy level lying just above the $^4\text{S}_{3/2}$, to obtain the green, red and near-infrared emissions originating from this $^4\text{S}_{3/2}$ level (after $^2\text{H}_{11/2}$ to $^4\text{S}_{3/2}$ non-radiative multiphonon relaxation) and from the $^4\text{F}_{9/2}$ level (after $^4\text{S}_{3/2}$ to $^4\text{F}_{9/2}$ multiphonon relaxation), then by exciting the sample at about 968 nm and 1475 nm in the $^4\text{I}_{11/2}$ and $^4\text{I}_{13/2}$ levels, respectively.

The results are reported in Fig. 5. These results are given in arbitrary units but each emission spectrum was corrected for the local spectral response of the registration apparatuses. As expected, after excitation at 519 nm, emissions are detected in the green, in the red (in agreement with [19] but with an improved spectral resolution) and in the near-infrared spectral regions, the most intense one occurring in the green around 545 nm and being assigned to a $^4\text{S}_{3/2} \rightarrow ^4\text{I}_{15/2}$ emission transition. On the other hand, exciting at 968 nm or 1475 nm only gave rise to a significant emission around 1545 nm, the one is clearly assigned to a

${}^4I_{13/2} \rightarrow {}^4I_{15/2}$ emission transition, this without detecting any trace of ${}^4I_{11/2} \rightarrow {}^4I_{15/2}$ emission around 990 nm, thus favoring the hypothesis of an efficient ${}^4I_{11/2} \rightarrow {}^4I_{13/2}$ non-radiative multiphonon relaxation process.

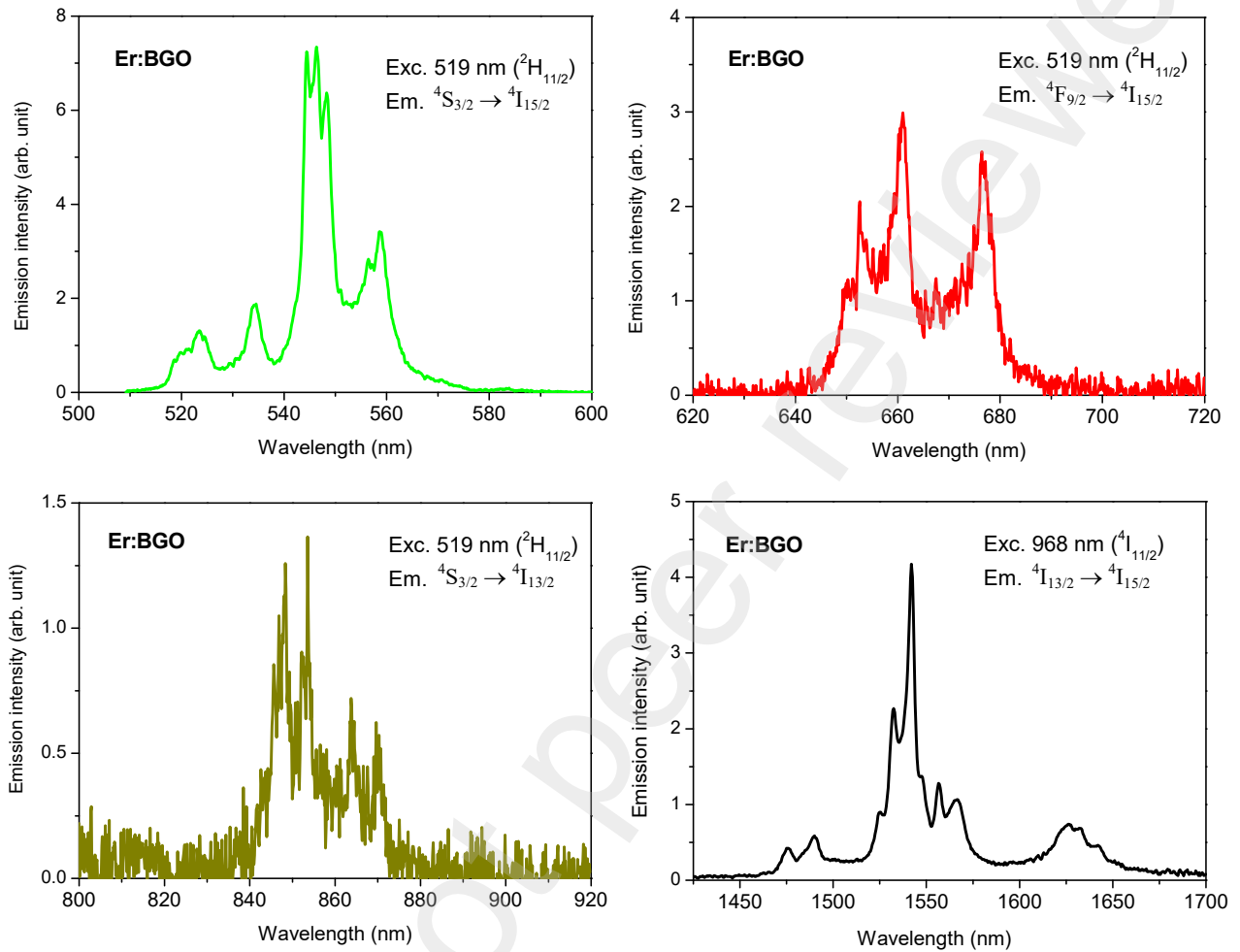


Fig. 5. Emission spectra of 0.5%Er:BGO registered either by exciting the sample at 519 nm (${}^2H_{11/2}$ level) or at 968 nm (${}^4I_{11/2}$)

In the case of **Tm:BGO** (see in Fig. 4), the most important emission transitions should come from the 1D_2 , 1G_4 , 3H_4 and 3F_4 levels. According to the branching ratios reported in Table 2, the first two levels should give rise to significant emissions (β above about 10%) around 370 nm (${}^1D_2 \rightarrow {}^3H_6$ transition), 460 nm (${}^1D_2 \rightarrow {}^3F_4$), 482 nm (${}^1G_4 \rightarrow {}^3H_6$ transition), 790 nm (${}^1G_4 \rightarrow {}^3H_5$ transition) and 1205 nm (${}^1G_4 \rightarrow {}^3H_4$ transition). The latter (3H_4 and 3F_4) should lead to emissions around 805 nm (${}^3H_4 \rightarrow {}^3H_6$), 1460 nm (${}^3H_4 \rightarrow {}^3F_4$) and 1850 nm (${}^3F_4 \rightarrow {}^3H_6$). No emission is expected from the 3H_5 level because of 3H_5 to 3F_4 non-radiative multiphonon relaxation.

The results are reported in Fig. 6. In agreement with the above expectations, intense emissions do occur in the blue, near-infrared and mid-infrared spectral domains at the expected emission wavelengths. Rather curiously, however, only very weak emissions could be detected (thus not reported in Fig. 6) around 370 nm (after 1D_2 level excitation around 353 nm) and around 1205 nm (after 1G_4 level excitation around 461 nm). Such a discrepancy is tentatively attributed to some inadequacy of the Judd-Ofelt formalism in the description of the branching

ratios of these 1D_2 and 1G_4 high lying energy levels, i.e. excited levels associated with wavefunctions which are strongly mixed with the BGO host-lattice ones. As we shall see in the following section, such a situation is also reflected in the discrepancy observed between the radiative and intrinsic emission lifetimes of these levels.

The emission spectra peaking around 1460 nm ($^3H_4 \rightarrow ^3F_4$) and 1825 nm ($^3F_4 \rightarrow ^3H_6$) were already partly reported in a previous paper [31]. We report them here again over more complete wavelength ranges and for sake of clarity.

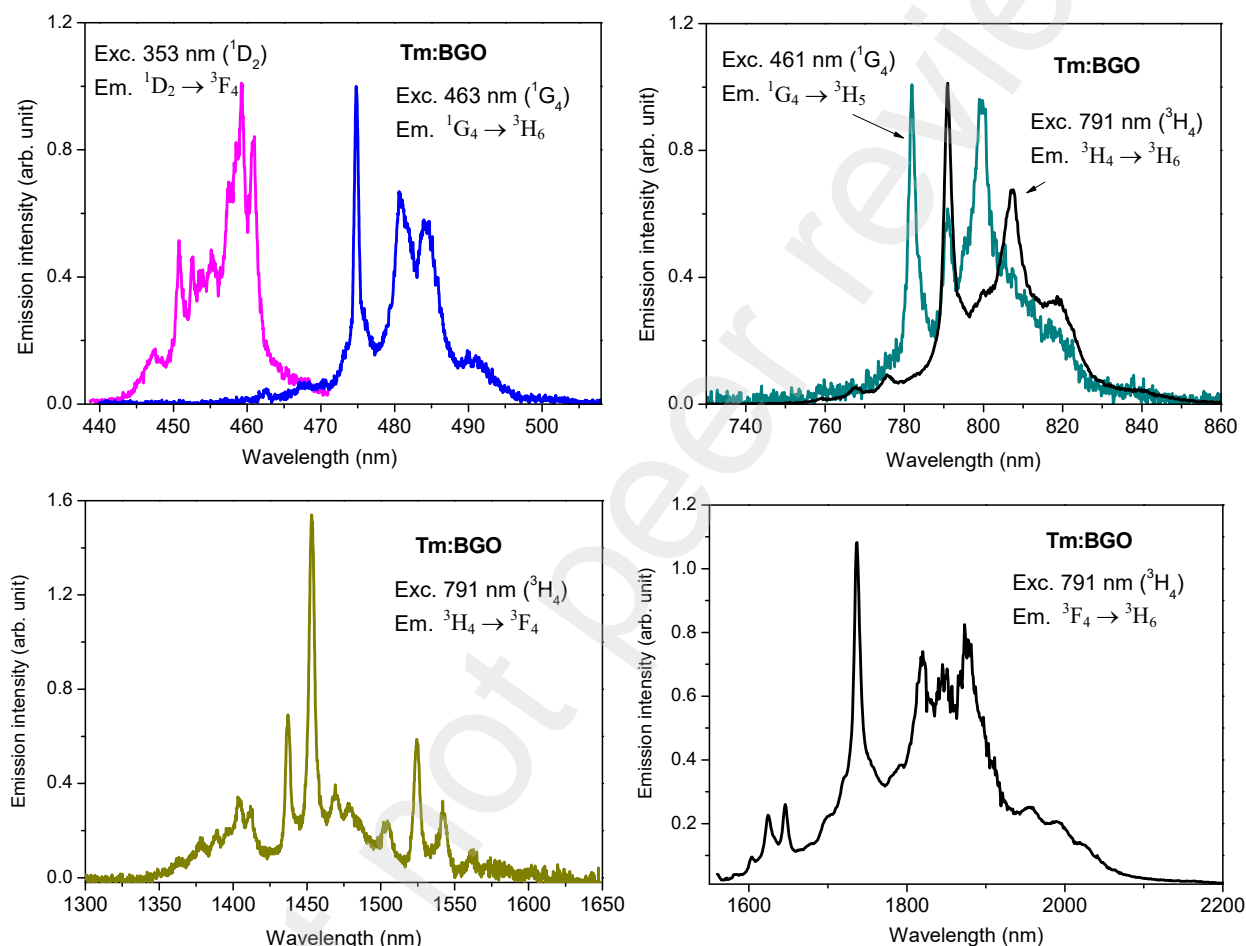


Fig. 6. Emission spectra of 0.5%Tm:BGO registered by exciting the sample at about 353 nm (1D_2), 461 nm (1G_4) and 791 nm (3H_4)

In the case of **Ho:BGO** (see in Fig. 4), the most important emissions should come the ($^5F_4, ^5S_2$), 5F_5 , 5I_6 and 5I_7 levels. According to the branching ratios reported in Table 3, the two first ones should lead to emissions around 545 nm ($^5F_4, ^5S_2 \rightarrow ^5I_8$), 664 nm ($^5F_5 \rightarrow ^5I_8$), 749 nm ($^5F_4, ^5S_2 \rightarrow ^5I_7$) and 966 nm ($^5F_5 \rightarrow ^5I_7$). The 5I_6 and 5I_7 levels should give rise to emissions around 1190 nm ($^5I_6 \rightarrow ^5I_8$), 1980 nm ($^5I_7 \rightarrow ^5I_8$) and 2941 nm ($^5I_6 \rightarrow ^5I_7$). We only report in Fig. 7 the emission spectra of the transitions which really occur with significant intensities.

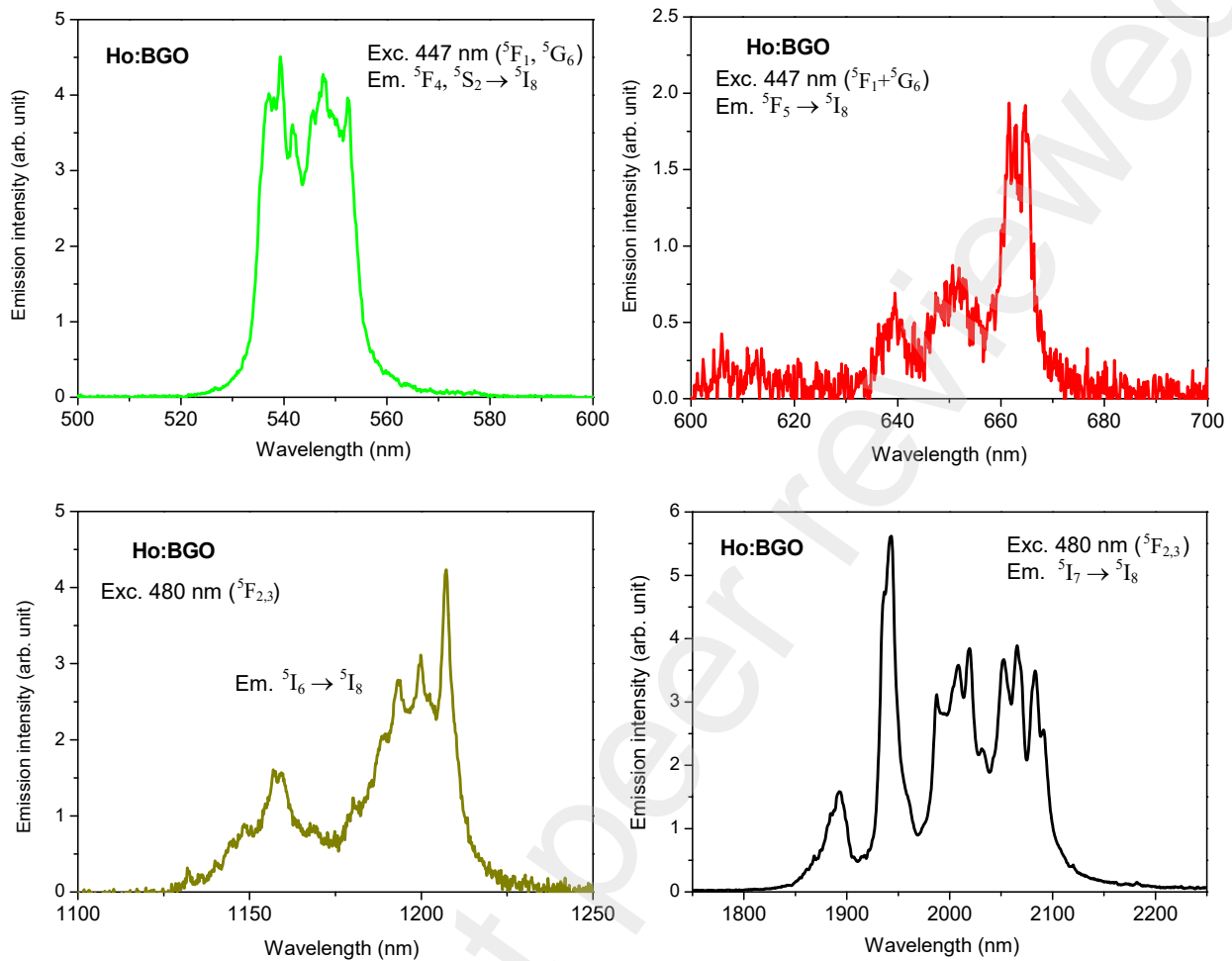


Fig. 7. Emission spectra of 0.5%Ho:BGO registered by exciting the sample at 447 nm ($^5F_1+^5G_6$ level) and 480 nm ($^5F_2+^5F_3$ level).

5. Emission lifetimes and non-radiative relaxation considerations

5.1. Fluorescence decay measurements

The $^4I_{13/2}$ fluorescence decay (~ 1545 nm) of the 0.5%Er-doped crystal was registered after direct $^4I_{13/2}$ (~ 1475 nm) and indirect $^4I_{11/2}$ (~ 968 nm) pulsed laser excitations. After direct excitation, the $^4I_{13/2}$ fluorescence decays exponentially with a time-constant thus an emission lifetime equal to ~ 6.66 ms. After indirect excitation, the fluorescence rises first with a time-constant of about 155 μ s, then decays exponentially with the same time-constant of 6.66 ms. This means that the $^4I_{11/2}$ excited level emission lifetime is equal to ~ 155 μ s. This is confirmed by registering the emission decay of this $^4I_{11/2}$ emitting level ($^4I_{11/2} \rightarrow ^4I_{15/2}$ emission transition at ~ 990 nm) and by exciting it either directly (~ 968 nm) or indirectly via the above lying level $^4I_{9/2}$ (~ 804 nm).

Fluorescence decay curves were also recorded by exciting the $^2H_{11/2}$ level (~ 519 nm) and by monitoring the emission intensity of the $^4S_{3/2}$ level at 546 nm ($^4S_{3/2} \rightarrow ^4I_{15/2}$ emission transition) and 850 nm ($^4S_{3/2} \rightarrow ^4I_{13/2}$ emission transition), then by monitoring the emission intensity of $^4F_{9/2}$ level at 663 nm ($^4S_{3/2} \rightarrow ^4I_{15/2}$ emission transition). Whereas both $^4S_{3/2}$ fluorescence decays exhibit a simple single-exponential behavior with a fluorescence time-

constant thus an emission lifetime of $\sim 20 \mu\text{s}$ ($22 \mu\text{s}$ is reported in [21]), the ${}^4\text{F}_{9/2}$ fluorescence rises first with a time-constant of $\sim 1.9 \mu\text{s}$ then decays with the same time-constant of $20 \mu\text{s}$. It simply means that the ${}^4\text{F}_{9/2}$ emission lifetime is equal to $\sim 1.9 \mu\text{s}$. Such a rise and decay behavior is indeed found when the fluorescence time-constant of the considered emitting level (here ${}^4\text{F}_{9/2}$) is shorter than the fluorescence decay of the above lying excited and feeding level (here ${}^4\text{S}_{3/2}$) [48]. This can be easily accounted for by solving a simple rate equation system. The result shows that after a ${}^4\text{S}_{3/2}$ excitation, the ${}^4\text{F}_{9/2}$ fluorescence intensity is proportional to:

$$N_2 = \frac{A_{32}N_3^0}{1/\tau_2 - 1/\tau_3} [\exp(-t/\tau_3) - \exp(-t/\tau_2)] \quad (1)$$

where N_2 stands for the ${}^4\text{F}_{9/2}$ excited population, N_3^0 the initial population of the ${}^4\text{S}_{3/2}$ excited energy level, A_{32} the ${}^4\text{S}_{3/2}$ to ${}^4\text{F}_{9/2}$ radiative + non-radiative relaxation rate, and τ_2 and τ_3 for the ${}^4\text{F}_{9/2}$ and ${}^4\text{S}_{3/2}$ emission lifetimes, respectively. As $\tau_2 < \tau_3$, the ${}^4\text{F}_{9/2}$ fluorescence decay curve rises first with the time-constant $\tau_2 = 1.9 \mu\text{s}$, then decays with the time-constant $\tau_3 = 20 \mu\text{s}$.

The same behavior is found in the case of Ho^{3+} (see in Fig. 4), when the fluorescence decay of the ${}^5\text{F}_5$ emitting level (with a derived emission lifetime of $0.75 \mu\text{s}$) is recorded after excitation of the above lying ${}^5\text{F}_4$ (${}^5\text{S}_2$) level (with a derived emission lifetime of $6.9 \mu\text{s}$), i.e. a ${}^5\text{F}_5$ fluorescence decay curve which rises first with the time-constant $\tau_2 = 0.75 \mu\text{s}$, then decays with the time-constant $\tau_3 = 6.9 \mu\text{s}$.

All the measured fluorescence lifetimes are reported in Table 4, along with those which were already reported in the literature [21, 22, 30, 31].

Table 4. Fluorescence lifetimes registered in the 0.5%Er-, 0.5%Tm- and 0.5%Ho-doped compounds and derived non-radiative relaxation rates for the most important emitting levels. Also put in parentheses “intrinsic” emission lifetimes extrapolated at zero-dopant concentrations (see in the text).

Emitting level (considered ion)	Energy gap ΔE (cm ⁻¹)	Fluorescence lifetime τ_F	Non-radiative relaxation rate W_{NR} (s ⁻¹)
${}^4\text{I}_{13/2}$ (Er ³⁺)	6081 [28]	6.7 ms, 8 ms [30]	-
${}^4\text{I}_{11/2}$ (Er ³⁺)	3378 [28]	155 μs	6.33×10^3
${}^4\text{F}_{9/2}$ (Er ³⁺)	2532 [28]	1.9 μs	5.25×10^5
${}^2\text{H}_{11/2}, {}^4\text{S}_{3/2}$ (Er ³⁺)	2886 [28]	20 μs , 23 μs [21]	5.1×10^4
${}^5\text{I}_7$ (Ho ³⁺)	4773	14 ms, 9 ms [30]	-
${}^5\text{I}_6$ (Ho ³⁺)	3050	70 μs	1.42×10^4
${}^5\text{F}_5$ (Ho ³⁺)	2227	0.75 μs	1.33×10^6
${}^5\text{F}_4, {}^5\text{S}_2$ (Ho ³⁺)	2845	6.9 μs	1.4×10^5
${}^3\text{F}_4$ (Tm ³⁺)	5340	5.5 ms [31], 6 ms [30]	-
${}^3\text{H}_4$ (Tm ³⁺)	3794	360 μs (444 μs), 402 μs [22]	1.25×10^3
${}^1\text{G}_4$ (Tm ³⁺)	6346	309 μs (360 μs)	-
${}^1\text{D}_2$ (Tm ³⁺)	6092	18 μs (20 μs)	-

5.2. Non-radiative multiphonon relaxation

To determine the non-radiative multiphonon relaxation contribution to the desexcitation rate of a particular emitting level at a given temperature, use is made of the following expression:

$$\frac{1}{\tau_{F0}} = \frac{1}{\tau_R^{eff}} + W_{NR} \quad (2)$$

where τ_R^{eff} stands for the purely radiative effective lifetime of the considered emitting level, τ_{F0} for its intrinsic emission lifetime, which is determined at low enough dopant concentration to neglect further excited-level relaxation due to inter-ionic energy transfers, and W_{NR} for the associated non-radiative multiphonon relaxation rate.

To perform such an investigation, it is thus necessary to check, for each considered emitting level, (1) that the radiative emission lifetime derived in Section 3 (via J.O. analysis of the absorption spectra) and reported in Tables 1-3 are “effective” radiative lifetimes, (2) that the measured fluorescence lifetimes reported in Table 4 for 0.5at% dopant concentrations are really “intrinsic” emission lifetimes.

Moreover, according to the so-called “energy gap law” [49], the non-radiative multiphonon relaxation rate W_{NR} would obey (under the assumption of weak electron-phonon coupling, which is generally the case for trivalent rare-earth ions) the following exponential expression:

$$W_{NR} = C \cdot \exp(-\alpha \cdot \Delta E) \quad (3)$$

where C and α are constants characteristic of the particular host material (C is an electronic factor and α measures the strength of the electron-phonon coupling) and ΔE measures the energy gap between the various emitting levels and their next lower energy levels.

Additionally, it was demonstrated that this non-radiative relaxation rate W_{NR} would be nearly negligible for energy gaps larger than about 5 times the highest phonon energies. Therefore, as the phonon energies which characterize BGO do not exceed some 900 cm^{-1} , W_{NR} should be negligible for all the emitting levels associated with energy gaps ΔE exceeding about 4500 cm^{-1} , thus according to the data reported in Table 4, for all the emitting levels $^4I_{13/2}$ (Er^{3+}), 5I_7 (Ho^{3+}), 3F_4 (Tm^{3+}), 1G_4 (Tm^{3+}) and 1D_2 (Tm^{3+}).

Consequently our analysis of the non-radiative multiphonon relaxation rates versus the energy gaps was restricted to the other emitting levels reported in Table 4, i.e. $^4I_{11/2}$ (Er^{3+}), $^4F_{9/2}$ (Er^{3+}), $^2H_{11/2}$, $^4S_{3/2}$ (Er^{3+}), 5I_6 (Ho^{3+}), 5F_5 (Ho^{3+}), 5F_4 , 5S_2 (Ho^{3+}), and 3H_4 (Tm^{3+}). However, among all these levels, only the fluorescence lifetimes measured at 0.5%at concentrations and reported for the $^4I_{11/2}$ (Er^{3+}), $^4F_{9/2}$ (Er^{3+}), 5I_6 (Ho^{3+}) and 5F_5 (Ho^{3+}) levels can be considered as “**intrinsic**” emission lifetimes (negligible contributions from energy-transfers) and their radiative lifetimes (as reported in Tables 1-3) can be considered as “**effective**” radiative lifetimes. It is not the case of the emitting levels $^2H_{11/2}$, $^4S_{3/2}$ (Er^{3+}) and 5F_4 , 5S_2 (Ho^{3+}) which are thermalized at room temperature and for which it is necessary to determine some “effective” radiative lifetimes. It is not the case either of the emitting level 3H_4 (Tm^{3+}) which is usually subject to rather strong cross-relaxation energy transfers, even at 0.5% Tm^{3+} dopant concentrations. The joint emitting levels $^2H_{11/2}$, $^4S_{3/2}$ (Er^{3+}) also experience cross-relaxation energy transfers but they can be considered as negligible since their emission lifetime only varies from 20 μs to 23 μs [21] for dopant concentrations going from 0.5% down to 0.1% Er^{3+} .

So, Concerning first the (${}^2H_{11/2}, {}^4S_{3/2}$) and (${}^5F_4, {}^5S_2$) emitting levels of the Er^{3+} and Ho^{3+} ions, (see in the Figs 2 and 3), the measured (thermalized) emission lifetimes should be compared with effective radiative lifetimes which can be determined by using the expression :

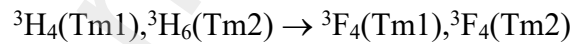
$$\frac{1}{\tau_R^{eff}} = \frac{g_1 \sum_i A_{1,i} + g_2 \sum_j A_{2,j} e^{-\Delta E/kT}}{g_1 + g_2 e^{-\Delta E/kT}} \quad (4)$$

where the indices 1 and 2 stand for the considered energy levels ($1 \equiv {}^4S_{3/2}$ or 5S_2 and $2 \equiv {}^2H_{11/2}$ or 5F_4), g_1 and g_2 for their degeneracies, ΔE for their energy separations and $A_{1,i}$ and $A_{2,j}$ for their transition rates to all the below lying energy levels.

Thus, using the data reported in Table 1 and Table 3 and energy separations of about 800 cm^{-1} and 140 cm^{-1} , respectively, it is found a (${}^2H_{11/2}, {}^4S_{3/2}$) effective radiative lifetime of about $751 \mu\text{s}$ (instead of 1.06 ms for ${}^4S_{3/2}$ alone) and a (${}^5F_4, {}^5S_2$) effective radiative lifetime of about $543 \mu\text{s}$ (instead of 1.1 ms for 5S_2 alone).

Using these effective radiative lifetimes for levels (${}^2H_{11/2}, {}^4S_{3/2}$) and (${}^5F_4, {}^5S_2$) and the radiative lifetimes reported in Table 1 and Table 3 for levels ${}^4I_{11/2}$ (Er^{3+}), ${}^4F_{9/2}$ (Er^{3+}), 5I_6 (Ho^{3+}) and 5F_5 (Ho^{3+}) as τ_R , then the measured emission lifetimes reported in Table 4 as τ_{F0} , it is found (by using Expr. (2)) the W_{NR} values reported in Table 4.

Concerning the case of the 3H_4 (Tm^{3+}) emitting level, the ‘‘intrinsic’’ emission lifetime was derived from a specific analysis of the fluorescence decays registered in a series of BGO samples doped with various amounts of Tm^{3+} ions (0.5%, 0.75%, 1%, 1.5% and 2%Tm). The 3H_4 fluorescence lifetime thus measured at about 1453 nm decreases from about $360 \mu\text{s}$ (for 0.5%Tm:BGO) down to about $215 \mu\text{s}$ (in 2%Tm:BGO), while that for the 3F_4 fluorescence remains approximately constant with a value of about 5.52 ms . The latter is very close to the 5.63 ms radiative emission lifetime derived from our J.O. analysis (see in Table 2) which means that neither Tm-Tm inter-ion energy transfers nor non-radiative (NR) intra-ion multiphonon relaxations affect the deactivation of the 3F_4 emitting level. On the other hand, the relatively small but non-negligible variation of the 3H_4 fluorescence lifetime is due to the above mentioned cross-relaxation energy transfers between neighboring Tm^{3+} ions. This well-known type of energy transfer can be written as :



which means that an ion Tm1 in its excited state 3H_4 transfers part of its energy to a neighboring ion Tm2 what brings both ions in their respective excited levels 3F_4 .

In principle, this should give rise to a nearly 200% quantum efficiency when the Tm-doped systems are pumped with 790 nm photons (into their 3H_4 energy level) and they are lased around $1.9 \mu\text{m}$ (from their 3F_4 metastable level).

According to theory and depending on host materials, the fluorescence lifetime of the 3H_4 emitting level $\tau_F^{3H_4}$ measured at high dopant concentrations should follow the expression:

$$\frac{1}{\tau_F} \approx \frac{1}{\tau_{F0}} + W_{CR} \quad (5)$$

where $\tau_{F0}^{3H_4}$ stands for the intrinsic emission lifetime (in the limit of very low Tm^{3+} dopant concentrations) and where the CR energy transfer rate W_{CR} increases quadratically with the doping concentration N_{Tm} (number of ions per cm^3) according to the relation [50] :

$$W_{CR} = C_{CR} \cdot N_{Tm}^2 \quad (6)$$

A plot of the inverse of the 3H_4 fluorescence lifetime measured in the singly doped Tm:BGO crystals versus dopant concentration is shown in Fig. 8 to illustrate this behavior. The fit to the data leads to $C_{CR}^{3H_4} \approx 4.8 \times 10^{-38} \text{ cm}^6\text{s}^{-1}$ and $\tau_{F0}^{3H_4} \approx 444 \text{ } \mu\text{s}$ (value put in parentheses in Table 4). The $C_{CR}^{3H_4}$ value thus found for Tm:BGO is very close to that found in the case of Tm:YAP [51].

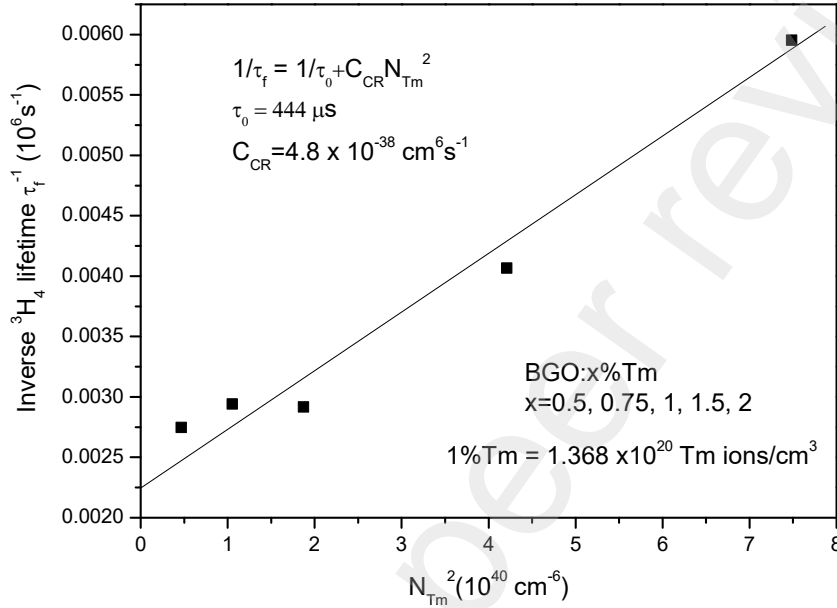
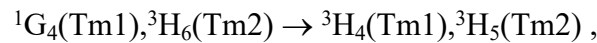
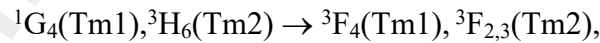
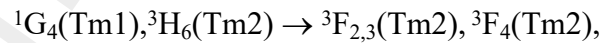
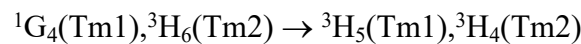


Fig. 8. Plot of the inverse of the average ${}^3H_4 \rightarrow {}^3F_4$ fluorescence lifetime measured in the singly doped Tm:BGO crystals versus the square of the Tm concentration (with 1at%Tm $\equiv 1.368 \times 10^{20} \text{ Tm}^{3+}$ ions/cm³).

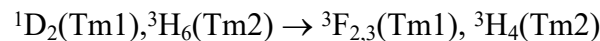
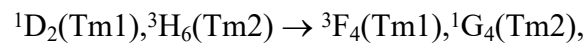
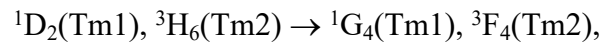
It is worth noting here that the same type of variations were observed with the fluorescence lifetimes of the 1G_4 and 1D_2 emitting levels measured at about 480 nm (after 462 nm excitation) and 458 nm (after 353 nm excitation), respectively. The first one (1G_4 emitting level) is due to four distinct but non-discernable, nearly-resonant, cross-relaxation type energy transfers which can be written (see in Fig. 2) as :



and



The second one (1D_2 emitting level) is also due to four non-discernable, nearly-resonant, cross-relaxation type energy-transfers which can be written as



and ${}^1D_2(\text{Tm}1), {}^3H_6(\text{Tm}2) \rightarrow {}^3H_4(\text{Tm}1), {}^3F_{2,3}(\text{Tm}2)$.

All these energy transfers involve spin-forbidden transitions. This is probably the reason why their combined effects do not affect so much the 1G_4 and 1D_2 emission lifetimes (see in the following), not more than the single type of energy transfers involving only spin-allowed transitions and affecting the 3H_4 emitting level. The 1G_4 fluorescence lifetime indeed decreases from 309 μs down to 186 μs , and the 1D_2 decreases from 18 μs down to 12.3 μs , when going from 0.5%Tm to 2%Tm dopant concentrations. As above, the inverse of the fluorescence lifetimes plotted in a semi-log scale versus the square of the dopant concentration lead to straight lines and fits of the data with the above expressions (5) and (6) lead to intrinsic emission lifetimes (extrapolated zero-dopant concentration values) $\tau_{F0}^{1G_4} \approx 360 \mu\text{s}$ and $\tau_{F0}^{1D_2} \approx 20 \mu\text{s}$ (values also reported in parentheses in Table 4), with the overall cross-relaxation energy transfer parameters $C_{CR}^{1G_4} \approx 3.5 \times 10^{-38} \text{ cm}^6\text{s}^{-1}$ and $C_{CR}^{1D_2} \approx 4.6 \times 10^{-37} \text{ cm}^6\text{s}^{-1}$, respectively.

In the end, use was made of the effective radiative lifetime determined above and reported in Tables 1-3 as well as the intrinsic fluorescence lifetimes reported in Table 4 to extract the non-radiative multiphonon rates versus the associated energy gaps reported in Table 4 and Fig. 9. Subsequent fits of these data to Expr. (3) (straight line in semi-log scale displayed in Fig. 9) thus led to the following parameters:

$$C \approx 4.2 \times 10^{10} \text{ s}^{-1} \text{ and } \alpha \approx 4.65 \times 10^{-3} \text{ cm}$$

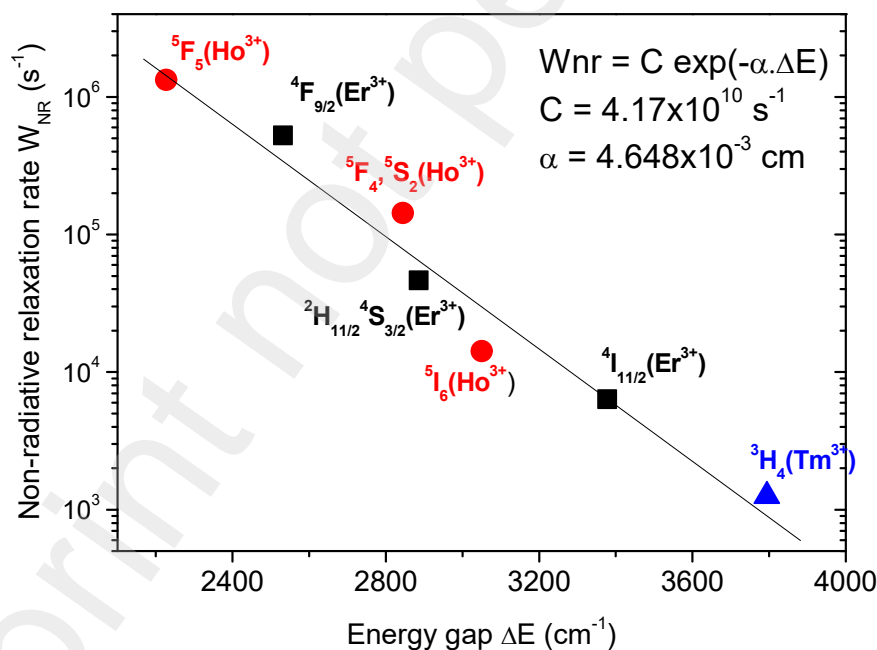


Fig. 9. Non-radiative multiphonon relaxation rate W_{NR} versus energy gap ΔE for a number of emitting levels of Er^{3+} , Tm^{3+} and Ho^{3+} -doped BGO

This result significantly differs from that derived from the theoretical data determined and reported in [28] in the case of Pr^{3+} -doped BGO, i.e. $C \approx 3.5 \times 10^{14} \text{ s}^{-1}$ and $\alpha = 7.85 \times 10^{-3} \text{ cm}$.

However, a comparable result was found in the case of rare-earth doped YVO_4 [52], another emitting crystalline oxide [53] for which the highest phonon energy which can be involved in

the electron-phonon coupling responsible for the non-radiative multi-phonon relaxation of the excited energy levels is around 950 cm^{-1} and W_{NR} is nearly negligible for energy gaps larger than about $950 \times 5 = 4750 \text{ cm}^{-1}$. Therefore, since, according to the results reported in Table 4 in the case of BGO, W_{NR} would be negligible for an energy gap of 4773 cm^{-1} (7I_7 to 5I_8 energy gap found in the case of Ho:BGO) but already non-negligible for an energy gap of 3794 cm^{-1} (case of the 3H_4 to 3H_5 energy gap found in Tm:BGO), it means that the highest phonon energies should be larger than about $3794/5 \approx 760 \text{ cm}^{-1}$ but smaller than $4773/5 \approx 950 \text{ cm}^{-1}$. This agrees well with the Raman and infrared spectra reported in [30, 38] which show phonons with energies up to about 820 cm^{-1} , thus slightly lower than in the case of YVO_4 . According to [38], these 820 cm^{-1} phonons would come from the coupling between the bending vibrations of the $(\text{GeO}_4)^{4-}$ tetrahedra and the vibrations corresponding to the motions of these $(\text{GeO}_4)^{4-}$ tetrahedra against the Bi^{3+} ions, thus the host ions for which the rare-earth dopants substitute.

6. Analysis and discussion of the results

Based on the results of the above investigation, it is now possible to discuss and decide the real potentialities of Er-, Tm- and Ho-doped BGO as laser materials, first in the mid-infrared domain, since it is in this spectral domain that they are supposed to give the best laser performances, but also in the visible and near-infrared.

6.1. Laser potential of the mid-infrared emission transitions

The laser potential of the corresponding emission transitions was investigated via the calibration of the spectra in cross section unit (i.e. in laser gain per unit population inversion). For that purpose, use was made of two methods.

The first method, referred as the Reciprocity (RP) method, makes use of the expression [54]:

$$\sigma_{em}^{RP, u \rightarrow l}(\lambda) = \sigma_{abs}^{l \rightarrow u}(\lambda) \cdot \frac{Z_l}{Z_u} \cdot \exp \left[\left(\frac{1}{\lambda_{ZL}} - \frac{1}{\lambda} \right) hc / kT \right] \quad (7)$$

where λ_{ZL} (in nm unit) is the so-called “zero-line” (ZL) wavelength which corresponds to the energy difference between the lowest sub-levels of each multiplet of the transition, $Z_m = \sum_k g_k^m \exp(-E_k^m / kT)$ is the partition function of the multiplet m resulting from the energetic positions E_k^m of the Stark levels of this multiplet and of their degeneracy g_k^m .

The second method, often called Fuchtbauer-Ladenburg (FL) method, makes use of the well-known expression [54]:

$$\sigma_{em}^{FL, u \rightarrow l}(\lambda) = \frac{\lambda^5 \beta_R}{8\pi c n^2 \tau_R} \frac{I_{em}^{u \rightarrow l}(\lambda)}{\int \lambda I_{em}^{u \rightarrow l}(\lambda) d\lambda} \quad (8)$$

which applies for cubic as well as for isotropic crystals (no polarization effect) and in which u and l stand for the upper and lower levels of the considered emission transition. $I_{em}(\lambda)$ is the

emission intensity and τ_R and β_R are the above derived (J.O. analysis) radiative emission lifetimes and branching ratios.

An alternative method to the FL method, also called β - τ method, consists in applying the same expression (8) but using as τ_R the most meaningful value between the emission lifetime measured at low dopant concentration (intrinsic fluorescence lifetime) and the radiative lifetime derived from the J.O. analysis, or the value which gives the best agreement with the emission spectrum derived with the RP method.

The resulting cross section spectra for the ${}^4I_{13/2} \rightarrow {}^4I_{15/2}$ emission of Er:BGO around 1.55 μm , for the ${}^3F_4 \rightarrow {}^3H_6$ emission of Tm:BGO around 1.9 μm and for the ${}^5I_7 \rightarrow {}^5I_8$ emission of Ho:BGO around 2 μm (all of them being ground-state terminating transitions associated with $\beta_R = 1$) are reported in the figures 10, 11 and 12.

Case of Er:BGO

In the case of the ${}^4I_{13/2} \rightarrow {}^4I_{15/2}$ emission of Er:BGO (see in the left side of Fig. 10), the emission cross section spectrum obtained by using the RP method was built by using (according to the energy-level positions indicated in [30]) the ZL wavelength $\lambda_{ZL} = 1540$ nm and the calculated partition functions are $Z_{{}^4I_{13/2}} = 7.80$ and $Z_{{}^4I_{15/2}} = 8.06$.

Alternatively the emission cross section spectrum obtained by using the FL expression (8) and which best fit with the short-wavelength part, the most reliable part in terms of noise, of that obtained with the previous RP method, was obtained by using the measured emission lifetime $\tau_F \approx 6.7$ ms instead of $\tau_R \approx 7.1$ ms.

To complete this analysis of the laser potential of Er:BGO we also show on the right hand side of Fig. 10 the gain cross section spectra $\sigma_{gain}(\lambda)$ which can be calculated from the above emission and absorption cross section spectra $\sigma_{em}(\lambda)$ and $\sigma_{abs}(\lambda)$ by using the expression:

$$\sigma_{gain}(\lambda) = \beta \cdot \sigma_{em}(\lambda) - (1 - \beta) \sigma_{abs}(\lambda) \quad (9)$$

for different values of the inversion population ratio $\beta = \frac{N_{{}^4I_{13/2}}}{N_{{}^4I_{13/2}} + N_{{}^4I_{15/2}}}$.

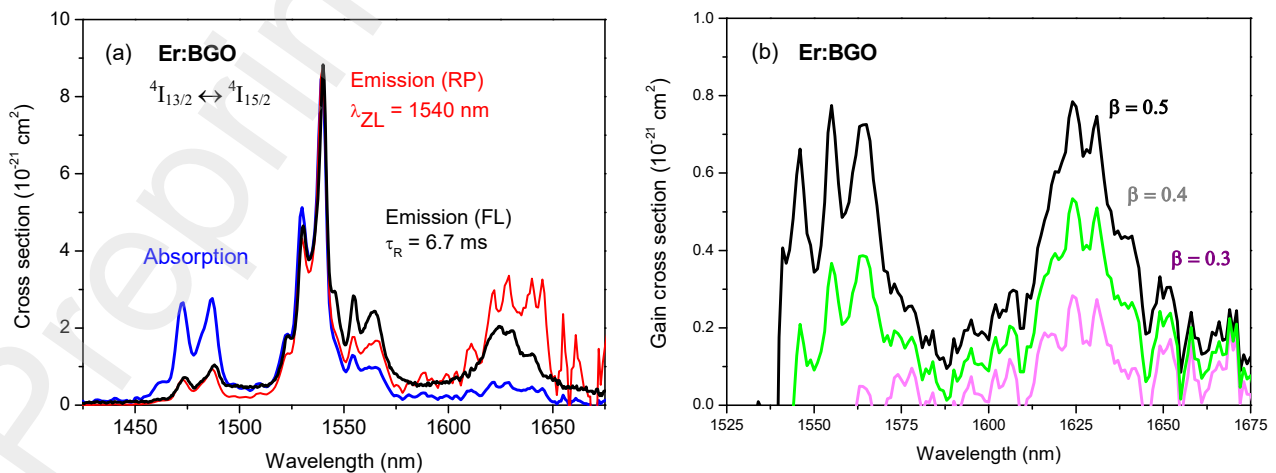


Fig. 10. (a) ${}^4I_{13/2} \rightarrow {}^4I_{15/2}$ emission cross section spectrum of Er:BGO obtained by using the FL expression (curve in black) and emission cross section spectrum (curve in red) built from the associated ${}^4I_{15/2} \rightarrow {}^4I_{13/2}$ absorption cross section spectrum (curve in blue) by using the RP method. (b) Calculated gain cross section spectra for various population inversion ratios.

These gain spectra show that laser action can be obtained with Er:BGO within two spectral ranges around 1560 nm and 1630 nm and with gain cross sections comparable to that found with the Er phosphate glass [55] which is the reference material in this eye-safe and telecom wavelength domain.

Case of Tm:BGO

In the case of Tm:BGO, it is clear that the zero-line wavelength (see on the left side of Fig. 11) for the ${}^3F_4 \leftrightarrow {}^3H_6$ emission and absorption transitions occurs at about 1737 nm (sharp peak observed both in the absorption and emission spectra), but no information is available about the Stark level structures of the considered multiplets which could allow for the derivation of the adequate Z_l/Z_u value. Therefore, considering the values which can be found in the literature with various Tm-doped fluorides and oxides, choice was made of the intermediate value $Z_l/Z_u \approx 1$, a value which is close to that found for instance in the case of $YAlO_3$ (YAP) or BaY_2F_8 [54]. The emission cross section spectrum thus obtained by using the RP method and that obtained by using the FL method with the 3F_4 radiative emission lifetime $\tau_R \approx 5.52$ ms (as derived from the J.O. analysis) are reported in Fig. 11.

The perfect agreement found between the emission cross section spectra obtained by the FL and RP methods thus clearly comforts the value of the 3F_4 radiative lifetime of 5.52 ms which is found via the J.O. formalism.

As previously, we also show on the right hand side of Fig. 11 the gain cross section spectra

$\sigma_{gain}(\lambda)$ which can be calculated by using Expr. (9) with $\beta = \frac{N_{{}^3F_4}}{N_{{}^3F_4} + N_{{}^3H_6}}$. It is found a

broad band with a maximum gain about 4 times lower than in the case of Tm:sesquioxides [56], but equivalent to that found with the reference material Tm:LiYF₄ [57].

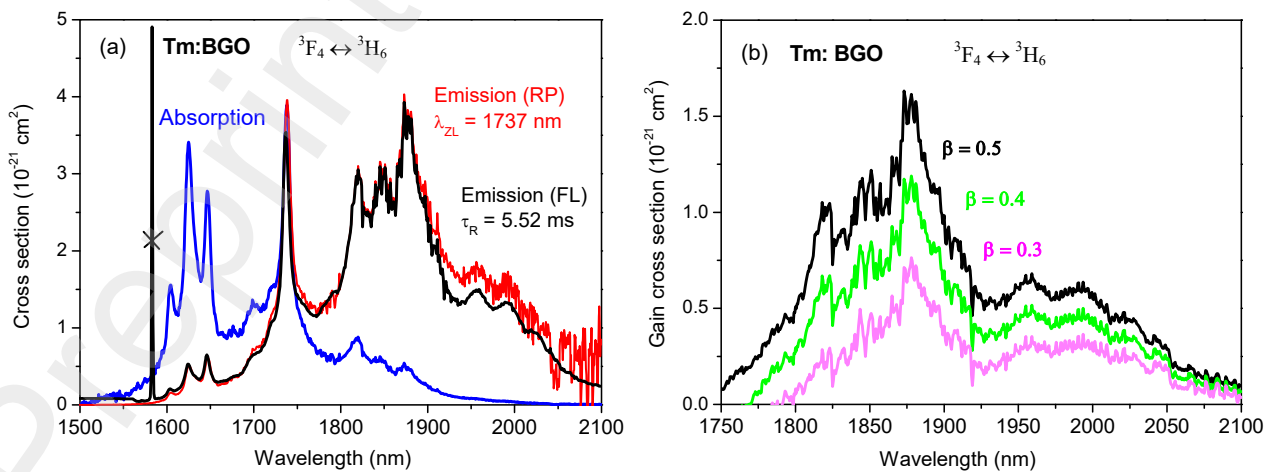


Fig. 11. (a) ${}^3F_4 \rightarrow {}^3H_6$ emission cross section spectrum of Tm:BGO obtained by using the FL expression (curve in black) and emission cross section spectrum (curve in red) built from the associated ${}^3H_6 \rightarrow {}^3F_4$ absorption cross section spectrum (curve in blue) by using the RP method (sharp peak at 1583 nm = grating 2nd order of the laser excitation at 791.5 nm). (b) Calculated gain cross section spectra for various population inversion ratios.

Case of Ho:BGO

In the case of the ${}^5I_7 \rightarrow {}^5I_8$ mid-infrared emission transition of **Ho:BGO** around 2 μm , as in the case of Tm:BGO, there is no information available about the Stark level structure of the considered 5I_7 and 5I_8 multiplets which allows for the determination of the adequate $Z_{s_{I_8}} / Z_{s_{I_7}}$ value. Thus, again, choice was made of an intermediate value [47, 54], i.e. $Z_{s_{I_8}} / Z_{s_{I_7}} \approx 0.8$. As to the zero-line wavelength, choice was made of the central wavelength of the strongest absorption peak, i.e. $\lambda_{ZL} \approx 1943$ nm. The resulting spectrum is reported in Fig. 12. It is also reported in Fig. 12 the emission cross section spectrum obtained by using the FL method with the 5I_7 radiative emission lifetime $\tau_R \approx 13.8$ ms. As in the case of Tm:BGO, the almost perfect agreement found between the emission spectra derived from the FL and RP methods clearly comfort the value of the 5I_7 radiative lifetime of about 13.8 ms which is found via the J.O. formalism.

As above, we also show on the right hand side of Fig. 12 the gain cross section spectra

$\sigma_{gain}(\lambda)$ which can be calculated by using Expr. (9), now with $\beta = \frac{N_{s_{I_7}}}{N_{s_{I_7}} + N_{s_{I_8}}}$.

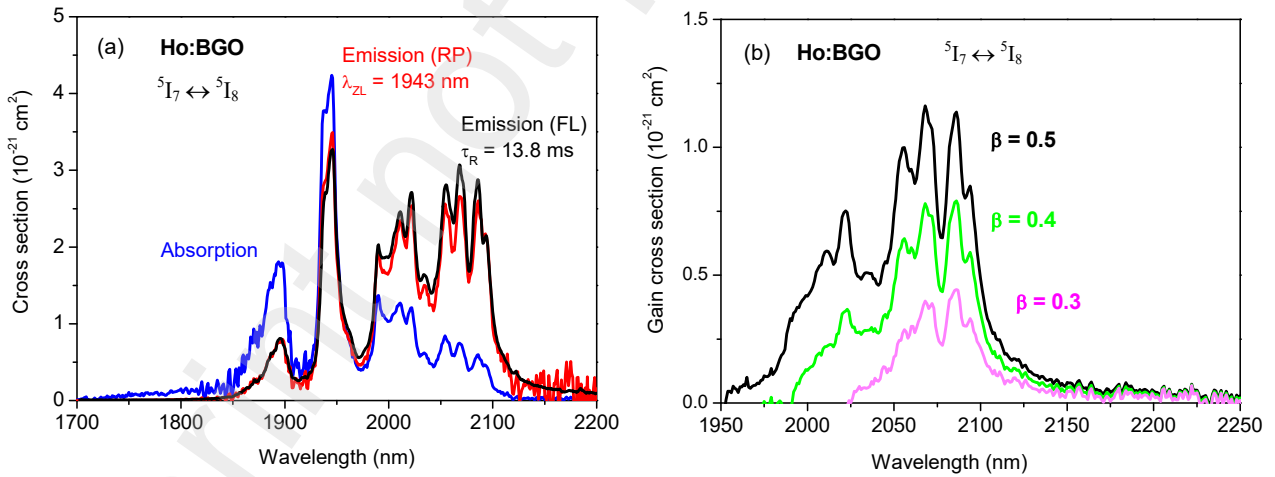


Fig. 12. (a) ${}^5I_7 \rightarrow {}^5I_8$ emission cross section spectra of Ho:BGO obtained by using the FL (curve in black) and RP (curve in red) expressions, along with the associated ${}^5I_8 \rightarrow {}^5I_9$ absorption cross section spectrum (curve in blue). (b) Calculated gain cross section spectra for various population inversion ratios.

It is found a maximum gain equivalent to that found in the case of the Ho doped Lu_2O_3 reference material [58] but shifted towards shorter wavelengths by about 50 nm.

6.2. Laser potential of the visible, deep-red and near-infrared emission transitions

The above discussed mid-infrared emission transitions all occur from the lowest (metastable) excited levels down to the ground-states of the considered emitting ions, thus correspond to branching ratios equal to unity. Moreover, none of them are subject to any energy transfer losses (at least for dopant concentrations up to a few at%) and all of them occur at energies larger than 5 times the highest phonon frequency, thus are not subject to any non-radiative multiphonon relaxations.

The situation is more complicated in the case of the other emission transitions because they all correspond to higher lying emission levels, thus having other lower energy levels than the ground-states towards which they can de-excite in a non-radiative way, and because they are associated with more or less important branching ratios never equal to unity. Moreover, at high dopant concentrations, a number of these emitting levels can be subject to various types of detrimental energy transfers.

Therefore, among all the emission transitions reported above, only few of them correspond to favorable conditions for laser operation and they are those coming from the 1D_2 , 1G_4 and 3H_4 emitting levels in Tm:BGO essentially, with the following characteristics:

- $^1D_2 \rightarrow ^3F_4$ emission transition around 457 nm with a branching ratio of 65% and an intrinsic emission lifetime of 20 μ s for a radiative lifetime of 38 μ s
- $^1G_4 \rightarrow ^3H_6$ and $^1G_4 \rightarrow ^3H_5$ emission transitions around 482 nm and 785 nm with branching ratios of 52% and 29%, an intrinsic emission lifetime of 360 μ s for a radiative emission lifetime of 585 μ s
- $^3H_4 \rightarrow ^3H_6$ and $^3H_4 \rightarrow ^3F_4$ emission transitions around 800 nm and 1450 nm with branching ratios of 85.5% and 11.5%, an intrinsic emission lifetime of 444 μ s and a radiative lifetime of 1 ms.

Calibrating the corresponding emission spectra reported in Figs 5, 6 and 7 using the above data and Expr. (8) leads to the peak emission cross sections reported in Table 5.

Table 5. Wavelengths and emission cross sections at the peaks of the most intense emission transitions observed in Tm:BGO in the visible, deep-red and near-infrared spectral regions.

Emission transition	$^1D_2 \rightarrow ^3F_4$	$^1G_4 \rightarrow ^3H_6$	$^1G_4 \rightarrow ^3H_5$	$^3H_4 \rightarrow ^3H_6$	$^3H_4 \rightarrow ^3F_4$
λ_{\max} (nm)	459	480.6	800	807	1453
$\sigma_{\text{em}}(\lambda_{\max}) 10^{-21} \text{ cm}^2$	32	1.4	2.9	4.4	5.5

Examining these data, several remarks can be made. It is to be noted first that all the considered emitting levels can be pumped directly by using standard laser sources, around 355 nm with frequency-tripled Nd-based solid-state lasers for level 1D_2 , around 462 nm with InGaN blue laser diodes for level 1G_4 , and around 792 nm with InGaAs near-infrared laser diodes for level 3H_4 . It is also remarked that two emission transitions ($^1G_4 \rightarrow ^3H_6$ and $^3H_4 \rightarrow ^3H_6$) are ground-state terminating transitions; thus, because of reabsorption effects, their effective laser emission wavelengths should be restricted to the long wavelength side of the spectra, i.e. around 590 nm for $^1G_4 \rightarrow ^3H_6$, and 820 nm for $^3H_4 \rightarrow ^3H_6$. In the end, it is also found that among the other three emission transitions, two of them ($^1D_2 \rightarrow ^3F_4$ and $^3H_4 \rightarrow ^3F_4$)

terminate on the long-lived (several milliseconds) metastable level 3F_4 , thus leading to so-called self-terminated laser transitions, while the third one ($^1G_4 \rightarrow ^3H_5$) terminates on the short-lived excited level 3H_5 . This means that a 4-level laser operation should be quite easy with this last emission transition but that an additional de-excitation process should be implemented to depopulate the 3F_4 metastable level in the case of the former two emission transitions. This is the reason why the near-infrared $^3H_4 \rightarrow ^3F_4$ emission transition was investigated in the past, more or less successfully, by co-doping the materials with Eu^{3+} , Tb^{3+} , Ho^{3+} or Yb^{3+} ions [59-70]. The 3F_4 excitation of the Tm^{3+} ions is indeed more or less efficiently transferred to these additional co-dopants, what shortens the 3F_4 lifetime and allows for true 4-levels laser operation. Tm^{3+} lasers emitting around 1.5 μm were thus demonstrated in (Tm^{3+} , Tb^{3+}), (Tm^{3+} , Ho^{3+}) and (Yb^{3+} , Tm^{3+}) doped LiYF_4 single crystals [59, 60, 64, 65, 67], but also in a (Tm^{3+} , Ho^{3+}) doped tellurite glass microsphere [68]. 3F_4 excitation quenching was also recently investigated with $\text{Tm}:\text{BGO}$ crystals co-doped with Pr^{3+} ions [69]. However, if Pr^{3+} ions do absorb and quench the 3F_4 excitation rather efficiently, they also substantially absorb at the $^3H_4 \rightarrow ^3F_4$ emission wavelengths around 1.5 μm , which is not very favorable. A better choice would be to co-dope the $\text{Tm}:\text{BGO}$ crystals again with Tb^{3+} or Yb^{3+} ions, what will be made in a near future.

7. Conclusions

A very complete investigation of the luminescence properties of Er^{3+} , Tm^{3+} and Ho^{3+} doped $\text{Bi}_4\text{Ge}_3\text{O}_{12}$ crystals prepared in the form of rod-type crystal fibers is reported here for the first time. It consists in the registration and the analysis of absorption and emission spectra as well as emission lifetimes in a wide spectral domain covering the blue to the mid-infrared. The effects of intra-levels thermalization, inter-ionic energy transfer and intra-ionic non-radiative multiphonon relaxation mechanisms affecting the measured emission lifetimes and quantum yields of the most important emitting levels are clearly identified. This leads to the determination of more reliable “effective” and “intrinsic” lifetimes. It also allows now unambiguously, thanks to the analysis of the experimentally derived multiphonon relaxation rates versus the energy gaps between the considered emitting levels and the excited levels lying just below, to assign the involved phonons to the high energy phonons of about 820 cm^{-1} which were evidenced in the past in the Raman and infrared spectra of the host material. Then, use is made of these data to calibrate the various emission spectra in cross section unit and to show that the considered materials do not only present an interest for the mid-infrared laser application but also in the blue and the near-infrared spectral regions.

These results finally open the way to the development of high power mid-infrared laser oscillators and amplifiers based on materials with a cubic crystallographic structure which can be easily prepared (low melting temperature) in the form of rod-type crystal fibers [71-73], thus of crystalline materials offering more robust thermo-mechanical properties than glass fibers, especially in the laser pulse regime, and more efficient thermal dissipation properties than standard bulk crystals. They also show the possibility of developing new broad-band, eventually tunable and/or short-pulse, laser sources in the blue, deep-red and near-infrared spectral domains by using different types of commercial solid-state and diode pump lasers.

Acknowledgments: The authors thank the supports of the State Scholarship Fund from China Scholarship Council (CSC) and the CNRS in France.

References

- [1] <https://www.crystals.saint-gobain.com/radiation-detection-scintillators/crystal-scintillators/bgo-bismuth-germanate#BGO> scintillator
- [2] M. J. Weber and R. R. Monchamp “Luminescence of $\text{Bi}_4\text{Ge}_3\text{O}_{12}$: Spectral and decay properties” *J. Appl. Phys.* **44**, 5495 (1973)
- [3] R. Moncorgé, B. Jacquier, G. Boulon, “Temperature dependent luminescence of $\text{Bi}_4\text{Ge}_3\text{O}_{12}$, discussion on possible models” *J. Lumin.* **14**, 337-348 (1976)
- [4] R. Moncorgé, B. Jacquier, G. Boulon, F. Gaume-Mahn, J. Janin, “Electronic structure and photoluminescence processes in $\text{Bi}_4\text{Ge}_3\text{O}_{12}$ single crystal”, *J. Lumin.* **12/13**, 467-472 (1976)
- [5] P. D. Marcillac, N. Coron, G. Dambier, J. Leblanc and J. P. Moalic, “Experimental detection of alpha-particles from the radioactive decay of natural bismuth”, *Nature* **422**, 876–878 (2003)
- [6] J. Chang, J. H. Adams, H. S. Ahn, G. L. Bashindzhagyan, M. Christl, O. Ganel, T. G. Guzik, J. Isbert, K. C. Kim, E. N. Kuznetsov, M. I. Panasyuk, A. D. Panov, W. K. H. Schmidt, E. S. Seo, N. V. Sokolskaya, J. W. Watts, J. P. Wefel, J. Wu and V. I. Zatsepin, “An excess of cosmic ray electrons at energies of 300–800 GeV,” *Nature*. **456**, 362-365 (2008)
- [7] H. Tsuchiya, T. Enoto, T. Torii, K. Nakazawa, T. Yuasa, S. Torii, T. Fukuyama, T. Yamaguchi, H. Kato, M. Okano, M. Takita and K. Makishima, “Observation of an Energetic Radiation Burst from Mountain-Top Thunderclouds,” *Phys. Rev. Lett.* **102**, 255003 (2009)
- [8] J.M. Classe, M. Fiche, C. Rousseau, C. Sagan, F. Dravet, R. Pioud, A. Lisbona, L. Ferrer, L. Campion, I. Resche, C. Curtet, “Prospective Comparison of 3 γ -Probes for Sentinel Lymph Node Detection in 200 Breast Cancer Patients,” *J. Nucl. Med.* **46** (3), 395-399 (2005)
- [9] T. H. Prettyman, D. W. Mittlefehldt, N. Yamashita, D. J. Lawrence, A. W. Beck, W. C. Feldman, T. J. McCoy, H. Y. Mc-Sween, M. J. Toplis, T. N. Titus, P. Tricarico, R. C. Reedy, J. S. Hendricks, O. Fomi, L. L. Corre, J. Y. Li, H. Mizzon, C. A. Raymond and C. T. Russell, “Elemental Mapping by Dawn Reveals Exogenic H in Vesta’s Regolith,” *Science* **338**, 242-246 (2012)
- [10] J. Du and T. Jones, “Technical opportunities and challenges in developing total-body PET scanners for mice and rats” *EJNMMI Physics* 10:2, 1-28 (2023)
- [11] J. Rodriguez, C. Belman-Rodriguez, S. A. Aguila, H. Liu, Y. Zhang and V. Pol, “Bismuth germanate ($\text{Bi}_4\text{Ge}_3\text{O}_{12}$), a promising high-capacity lithium-ion battery anode,” *Chem. Commun.* **54** (81), 11483-11486 (2018)
- [12] E. Moya, L. Contreras and C. Zaldo, “ $\text{Bi}_4\text{Ge}_3\text{O}_{12}:\text{Cr}$: a new photorefractive material,” *J. Opt. Soc. Am. B* **5** (8), 1737-1742 (1988)
- [13] L. Kovács, E. Moya, K. Polgár, F.J. Lopez and C. Zaldo, “Photochromic behaviour of doped $\text{Bi}_4\text{Ge}_3\text{O}_{12}$ single crystal scintillators,” *Appl. Phys. A* **52** 307-312 (1991)
- [14] C. Zaldo and E. Diéguez, “On the microscopic origin of the photochromic and photorefractive behavior of transition metal ion doped $\text{Bi}_4\text{Ge}_3\text{O}_{12}$ single crystals,” *Opt. Mater.* **1** (3), 171-176 (1992)
- [15] C. Zaldo, E. Moya, L. F. Magaña, L. Kovács, and K. Polgár, “Optically induced gratings in Fe and Mn doped $\text{Bi}_4\text{Ge}_3\text{O}_{12}$ single crystals” *J. Appl. Phys.* **73**, 2114 (1993)
- [16] Q. Song, X. Xu, J. Liu, X. Bu, D. Li, P. Liu, Y. Wang, J. Xu, and K. Lebbou, “Structure and white LED properties of Ce-doped YAG- Al_2O_3 eutectics grown by the micro-pulling-down method,” *Cryst. Eng. Comm.*, **21**, 4545-4550 (2019)
- [17] J.B. Shim, A. Yoshikawa, M. Nikl, and T. Fukuda, “ Eu^{3+} doped $\text{Bi}_4\text{Ge}_3\text{O}_{12}$ fiber crystals

- grown by the by the micro-pulling down method,” *J. Cryst. Growth* **245**, 67-72 (2002)
- [18] N. Li, Y. Xue, D. Wang, B. Liu, C. Guo, Q. Song, X. Xu, J. Liu, D. Li, J. Xu, Z. Xu, and J. Xu, “Spectroscopic properties of Eu:Bi₄Ge₃O₁₂ single crystal grown by the micro-pulling down method,” *J. Lumin.* **208**, 208-212 (2019)
- [19] B. Huang, B. Zhang, X. Qian, J. Wang, Q. Yang, L. Su, “Effects of Er³⁺ concentration on upconversion luminescence and temperature sensing properties in Bi₄Ge₃O₁₂ crystal” *J. of Alloys and Comp.* **853** 156970 (2021)
- [20] F. Chen, M. Ju, G. L. Gutsev, X. Kuang, C. Lu, Y. Yeung, “Structure and luminescence properties of the Nd³⁺ doped Bi₄Ge₃O₁₂ scintillation crystal: new insights from a comprehensive study”, *J. Mat. Chem. C* **5**, 3079-3087 (2017)
- [21] K. Okazaki, H. Fukushima, D. Nakauchi, G. Okada, D. Onoda, T. Kato, N. Kawaguchi, T. Yanagida, “Investigation of Er:Bi₄Ge₃O₁₂” single crystals emitting near-infrared luminescence for scintillation detectors” *J. Alloys & Comp.* **903**, 163834 (2022)
- [22] K. Okazaki, D. Nakauchi, H. Fukushima, T. Kato, N. Kawaguchi, and T. Yanagida, “Radiation-induced Luminescence Properties of Tm-doped Bi₄Ge₃O₁₂ Single Crystals” *Sensors and Materials* **35** (2) 459–466 (2023)
- [23] A.A. Kaminskii, D. Schultze, B. Hermoneit, S.E. Sarkisov, L. Li, J. Bohm, P. Reiche, R. Ehler, A.A. Mayer, V.A. Lomonosov, V.A. Balashov, “Spectroscopic Properties and Stimulated Emission in the ⁴F_{3/2}→⁴I_{11/2}, and ⁴F_{3/2}→⁴I_{13/2} Transitions of Nd³⁺ Ions from Cubic Bi₄Ge₃O₁₂ Crystals” *Phys. Stat. Sol. (a)* **33**, 737 (1976)
- [24] G. A. Kumar, R. E. Riman, A. A. Kaminskii, R. Praveena, C. K. Jayasankar, I. K. Bae, S. C. Chae, Y. N. Jang, “Optical properties of single crystal Nd³⁺-doped Bi₄Ge₃O₁₂: Laser transitions at room and low temperature”, *Phys. Rev. B* **74**, 014306 (2006)
- [25] H. Loro, D. Vasquez, E. Camarillo, H. del Castillo, I. Camarillo, G. Muñoz, C. Flores, J. Hernández, and H. Murrieta, S. “Experimental study and crystal-field modeling of Nd³⁺ (4/3) energy levels in Bi₄Ge₃O₁₂ and Bi₄Si₃O₁₂”, *Phys. Rev. B* **75**, 125405 (2007)
- [26] Y. Lin, Q. Wu, S. Wang, A. Wu, L. Su, L. Zheng, J. Chen, Z. Qin, G. Xie, X. Xu, Q. Song, and Q. Hang, “Growth and laser properties of Nd³⁺-doped Bi₄Ge₃O₁₂ single-crystal fiber,” *Opt. Lett.* **43** (6), 1219-1221 (2018)
- [27] N. Li, Y. Xue, D. Wang, B. Liu, C. Guo, Q. Song, X. Xu, J. Liu, D. Li, J. Xu, Z. Xu, and J. Xu, “Optical properties of Nd:Bi₄Ge₃O₁₂ crystals grown by the micro-pulling down method,” *J. Lumin.* **206**, 412-416 (2019)
- [28] A. A. Kaminskii, S. E. Sarkisov, G. A. Denisenko, V. V. Ryabchenkov, V. A. Lomonosov, Yu E. Perlin, M. G. Blazha, D. Schultze, B. Hermoneit, P. Reiche, “Growth, Spectral and Luminescence Study of Cubic Bi₄Ge₃O₁₂:Pr³⁺ crystals”, *Phys. Stat. Sol. (a)* **86**, 553 (1984)
- [29] J. Xu, Y. Guyot, K. Lebbou, Xiaodong Xu, Jian Liu, Jun Xu, R. Moncorgé, “Luminescence properties of Pr³⁺ doped Bi₄Ge₃O₁₂ crystal fibers grown by the micro-pulling down technique”, *J. Lumin.* **260**, 119882 (2023)
- [30] A. A. Kaminskii, S. E. Sarkisov, T. I. Butaeva, G. A. Denisenko, B. Hermoneit, J. Bohm, W. Grosskreut and D. Schultze, “Growth, Spectroscopy, and Stimulated Emission of Cubic Bi₄Ge₃O₁₂ crystals Doped with Dy³⁺, Ho³⁺, Er³⁺, Tm³⁺, or Yb³⁺ Ions”, *Phys. Stat. Sol. (a)* **56**, 725 (1979)
- [31] W. Lu, J. Xu, Q. Song, K. Bian, J. Guo, J. Liu, D. Li, P. Liu, C. Zhang, X. Xu, J. Xu, K. Lebbou, “Spectroscopic properties of Tm:Bi₄Ge₃O₁₂ crystals grown by the micro-pulling-down method”, *J. Lumin.* **238**, 118299 (2021)
- [32] D. P. Bortfeld and H. Meier, “Refractive indices and electrooptic coefficients of the eulitities Bi₄Ge₃O₁₂ and Bi₄Si₃O₁₂” *J. appl. Phys.* **43**, 5110 (1972)
- [33] P.A. Williams, A.H. Rose, K.S. Lee, D.C. Conrad, G.W. Day, and P.D. Hale, “Optical, thermo-optic, electro-optic, and photoelastic properties of bismuth germanate (Bi₄Ge₃O₁₂),”

Appl. Opt. **35** (19), 3562-3569 (1996)

[34] V. D. Golyshev · M. A. Gonik · V. B. Tsvetovskiy, “Spectral Absorptivity and Thermal Conductivity of BGO and BSO Melts and Single Crystals” *Int. J. Thermophys.* **29**, 1480–1490. (2008)

[35] H. Farhi, S. Belkahla, K. Lebbou, and C. Dujardin, “BGO fibers growth by μ -pulling down technique and study of light propagation,” *Phys. Procedia* **2**, 819-825 (2009)

[36] V. Chani, K. Lebbou, B. Hautefeuille, O. Tillement, and J. M. Fourmigue, “Evaporation induced diameter control in fiber crystal growth by micro-pulling-down technique: $\text{Bi}_4\text{Ge}_3\text{O}_{12}$,” *Cryst. Res. Technol.* **41**, 972-978 (2006)

[37] J.B. Shim, J.H. Lee, A. Yoshikawa, M. Nikl, D.H. Yoon, and T. Fukuda, “Growth of $\text{Bi}_4\text{Ge}_3\text{O}_{12}$ single crystal by the micro-pulling-down method from bismuth rich composition,” *J. Cryst. Growth* **243**, 157-163 (2002)

[38]. M. Couzi, J. R. Vignalou, G. Boulon “Infrared and Raman study of the optical phonons in $\text{Bi}_4\text{Ge}_3\text{O}_{12}$ single crystals” *Solid. State Comm.* **20**, 461-465 (1976)

[39]. A.K. Jazmati, P.D. Townsend, “Photoluminescence from RE doped BGO waveguides” *Nucl. Inst. and Meth. in Phys. Res. B* **166-167**, 597-601(2000)

[40] H. V. Philipsborn, “Croissance d'eulytine $\text{Bi}_4\text{Si}_3\text{O}_{12}$ et des composés substitués $\text{Bi}_4\text{Ge}_3\text{O}_{12}$ par la méthode Czochralski” *J. Cryst. Growth* **11**, 348 (1971)

[41] G.M. Kuz'micheva, I.A. Kaurova, L.I. Ivleva, E.V. Khramov, P.A. Eistrikh-Geller, V.B. Rybakov, T.V. Chukhlovina, S.V. Firstov, “Structure and composition peculiarities and spectral-luminescent properties of colorless and pink $\text{Bi}_4\text{Ge}_3\text{O}_{12}$ scintillation crystals” *Arabian Journal of Chemistry* **11** (8) (2017); doi:10.1016/j.arabjc.2017.07.015

[42] S.A.S. Farias, M.V. Lalic, “The local structure around the Nd impurity incorporated into the $\text{Bi}_4\text{Ge}_3\text{O}_{12}$ crystal matrix: An ab initio study” *Sol. St. Comm.* **150**, 1241-1244 (2010)

[43] M. J. Weber, “Probabilities for Radiative and Nonradiative Decay of Er^{3+} in LaF_3 ” *Phys. Rev.* **157** (2) 262 (1967)

[44] R. Moncorgé, Y. Guyot, C. Kränkel, K. Lebbou, A. Yoshikawa, “Mid-infrared emission properties of the Tm^{3+} -doped sesquioxide crystals Y_2O_3 , Lu_2O_3 , Sc_2O_3 and mixed compounds $(\text{Y,Lu,Sc})_2\text{O}_3$ around 1.5-, 2- and 2.3- μm ” *J. Lumin.* **241**, 118537 (2022) and refs therein

[45] M. J. Weber, B. H. Matsinger, V. L. Donlan, G. T. Surratt “Optical Transition Probabilities for Trivalent Holmium in LaF_3 and YAlO_3 ” *J. Chem. Phys.* **57**, 562 (1972)

[46] A.A. Kaminskii, “Laser Crystals, their physics and principles” *Springer Series in Optical Sciences* (1996)

[47] B. M. Walsh, N. P. Barnes, B. Di Bartolo, “Branching ratios, cross sections, and radiative lifetimes of rare earth ions in solids: Application to Tm^{3+} and Ho^{3+} ions in LiYF_4 ” *J. Appl. Phys.* **83** (5) 2772-2787 (1998)

[48] J. Rubin, A. Brenier, R. Moncorgé, C. Pedrini, “ $\text{Er}^{3+} \rightarrow \text{Ho}^{3+}$ energy transfer mechanisms at room temperature in YLiF_4 single crystals”, *J. Physique* **48**, 1761-1777 (1987)

[49] T. Miyakawa, D.L. Dexter, “Phonon Sidebands, Multiphonon Relaxation of Excited States, and Phonon-Assisted Energy Transfer between Ions in Solids”, *Phys. Rev.* **B1**, 2961(1970)

[50] J. A. Caird, A. J. Ramponi, and P. R. Staver, “Quantum efficiency and excited-state relaxation dynamics in neodymium-doped phosphate laser glasses”, *J. Opt. Soc. Am. B* **8**, 1391-1403 (1991)

[51] L. Guillemot, L. Pavel, A. Braud, J.L. Doualan, A. Hideur, M. Koselja, R. Moncorgé, P. Camy, “Continuous-wave $\text{Tm}:\text{YAlO}_3$ laser at $\sim 2.3 \mu\text{m}$ ” *Opt. Lett.* **44** (20), 5077-5080 (2019)

[52] F. S. Ermeneux, C. Goutaudier, R. Moncorgé, Y. Sun and R. L. Cone, E. Zannoni and E. Cavalli, M. Bettinelli, “Multiphonon relaxation in YVO_4 single crystals”, *Phys. Rev. B* **61** (6) 3915-3921 (2000)

- [53] C. Hsu and R. C. Powell, "Energy transfer in europium doped yttrium vanadate crystals" *J. Lumin.* **10**, 273-293 (1975)
- [54] S. A. Payne, L. L. Chase, L. K. Smith, W. L. Kway, and W. F. Krupke, "Infrared Cross - Section Measurements for Crystals Doped with Er^{3+} , Tm^{3+} , and Ho^{3+} ", *I.E.E.E. J. Quant. Electr.* **28** (11) 2619-2630 (1992)
- [55] Zh. Cai, A. Chardon, H. Xu, P. Feron, G.M. Stephan "Laser characteristics at 1535 nm and thermal effects of an Er:Yb phosphate glass microchip pumped by Ti:sapphire laser", *Optics Communications* **203**, 301-313(2002)
- [56] P. Loiko , Ph. Koopmann, X. Mateos , J. M. Serres, V. Jambunathan , A. Lucianetti, T. Mocek, M. Aguilo, F. Diaz, U. Griebner, V. Petrov and Ch. Krankel, "Highly Efficient, Compact $\text{Tm}^{3+}:\text{RE}_2\text{O}_3$ (RE = Y, Lu, Sc) Sesquioxide Lasers Based on Thermal Guiding" *IEEE Sel. Top. Quant. Electron.* **24** (5) 1600713 (2018)
- [57] P. Loiko, R. Soulard, G. Brasse, J. L. Douala, B. Guichard, A. Braud, A. Tyazhev, A. Hideur, P. Camy, "Watt-level Tm:LiYF₄ channel waveguide laser produced by diamond saw dicing, *Opt. Expr.* **26** (19) 24653 (2018)
- [58] P. Koopmann, S. Lamrini, K. Scholle, M. Schäfer, P. Fuhrberg, and G. Huber, "Multi-watt laser operation and laser parameters of Ho-doped Lu₂O₃ at 2.12 μm ", *Opt. Mater. Expr.* **1**, 1447 (2011)
- [59] R.C. Stoneman, and L. Esterowitz, "Continuous-wave 1.50- μm thulium cascade laser," *Opt. Lett.* **16** (4), 232-234 (1991)
- [60] G.H. Rosenblatt, R.C. Stoneman, L. Esterowitz, "Diode-pumped room-temperature CW Tm:Tb:YLF laser" *OSA Proc. ASSL'90*, H.P. Jenssen and G. Dube (eds) vol. **6**, pp 26-29 (1990)
- [61] W. Ryba-Romanowski, M. Berkowski, B. Viana, and P. Aschehoug, "Relaxation dynamics of excited states of Tm^{3+} in SrGdGa₃O₇ crystals activated with Tm^{3+} and $\text{Tm}^{3+} + \text{Tb}^{3+}$," *Appl. Phys. B* **64**, 525-529 (1997)
- [62] M. Bettinelli, F.S. Ermeneux, R. Moncorgé, and E. Cavalli, "Fluorescence dynamics of YVO₄: Tm^{3+} , YVO₄: $\text{Tm}^{3+}, \text{Tb}^{3+}$ and YVO₄: $\text{Tm}^{3+}, \text{Ho}^{3+}$ crystals," *J. Phys.: Condens. Matter* **10**, 8207-8215 (1998)
- [63] A. Braud, S. Girard, J.L. Doualan, and R. Moncorgé, "Spectroscopy and Fluorescence Dynamics of ($\text{Tm}^{3+}, \text{Tb}^{3+}$) and ($\text{Tm}^{3+}, \text{Eu}^{3+}$) Doped LiYF₄ Single Crystals for 1.5 μm Laser Operation," *IEEE J. Quantum Electron.* **34** (11), 2246-2255 (1998)
- [64] A. Diening, P. E.-A. Mobert, and G. Huber, "Diode-pumped continuous-wave, Quasi-continuous-wave, and Q-switched laser operation of ($\text{Yb}^{3+}, \text{Tm}^{3+}$): YLiF₄ at 1.5 and 2.3 μm ," *J. Appl. Phys.* **84** (11), 5900-5904 (1998)
- [65] A. Braud, S. Girard, J. L. Doualan, M. Thuau, and R. Moncorgé, "Energy-transfer processes in Yb:Tm-doped KY₃F₁₀, LiYF₄, and BaY₂F₈ single crystals for laser operation at 1.5 and 2.3 μm ", *Phys. Rev. B* **61** (8), 5280-5292 (2000)
- [66] P. Zhang, X. Huang, R. Wang, Z. Li, H. Yin, S. Zhu, Z. Chen, and Y. Hang, "Enhanced 1.4 μm emissions of Tm^{3+} via Tb^{3+} deactivation in ($\text{Gd}_{0.5}\text{Lu}_{0.5}$)₂SiO₅ crystal," *Opt. Mater. Express.* **8**(3), 668–675(2018)
- [67] A. Braud, M. Fromager, J.L. Doualan, S. Girard, R. Moncorgé, M. Thuau, B. Ferrand , Ph. Thony "Passive Q-switching and wavelength tunability of a diode-pumped Tm:Yb:YLiF laser around 1.5 μm ", *Opt. Comm.* **183**, 175–179 (2000)
- [68] A. Li, W. Li, M. Zhang, Y. Zhang, S. Wang, A. Yang, Z. Yang, and E. Lewis, G. Brambilla, and P. Wang, "Tm³⁺-Ho³⁺ codoped tellurite glass microsphere laser in the 1.47 μm wavelength region," *Opt. Lett.* **44**(3), 511-513 (2019)

- [69] Q. Li, J. Dong, Q. Wang, H. Zhao, Y. Xue, H. Tang, X. Xu, and J. Xu, "Growth and spectroscopic properties of Tm^{3+} and Tb^{3+} co-doped $GdScO_3$ crystal," *J. Lumin.* **230**, 117681 (2021)
- [70] W. Lu, Jie Xu, Q. Song, K. Bian, J. Guo, J. Liu, D. Li, P. Liu, C. Zhang, Xiaodong Xu, Jun Xu, K. Lebbou, "Pr³⁺ deactivation effect to Tm³⁺ at ~1.5 μm emission in $Bi_4Ge_3O_{12}$ crystals grown by the micro-pulling-down method" *J. Lumin.* **246**, 118829 (2022)
- [71] M. Dubinskii, J. Zhang, V. Fromzel, Y. Chen, S. Yin, C. Lu, "Low-loss 'crystalline-core/crystalline-clad'(C4) fibers for highly power scalable high efficiency fiber lasers" *Opt. Expr.* **26** (4) 5092-5101 (2018)
- [72] D. Sangla, I. Martial, N. Aubry, J. Didierjean, D. Perrodin, F. Balembois, K. Lebbou, A. Brenier, P. Georges, O. Tillement, J. M. Fourmigué, "High power laser operation with crystal fibers" *Appl Phys B* **97**, 263–273(2009)
- [73] N. Deguil-Robin, J. Limpert, I. Manek-Hönninger, F. Salin, F. Röser, A. Liem, T. Schreiber, S. Nolte, H. Zellmer, A. Tünnermann, J. Broeng, A. Petersson, C. Jakobsen, Rod-type fiber laser, *Adv. Sol.-State Phot. OSA/ASSP*, 511-515 (2005)